nature communications

Article | Article in Press

https://doi.org/10.1038/s41467-026-78000-2

Differential effects of visual and tactile deprivation on spatially modulated cells in the medial entorhinal cortex

Received: 17 September 2024

Accepted: 10 September 2026

Published online: 06 October 2026

Check for updates

Jiayi Tian[1,2], Shidan Wen[1,2], Yuqian Zhou[1,2], Nan Hu[1,2], Shuyang Yao[1,2], Xuan Zhang[1,2,3], Yuanjing Liu[1,2], Yuheng He[1,2], Zhouyuan Wang[1,2,3] & Chenglin Miao[1,2,3,4,5,6]

Spatial navigation requires internal maps to remain anchored to external sensory cues. The medial entorhinal cortex (MEC) contains spatially modulated cell types, but how visual and tactile cues jointly support them is unclear. Here we show, using miniature two-photon calcium imaging in freely moving male mice, that sensory deprivation has context-dependent effects. In a visually dominated environment, darkness disrupted all spatially modulated cell types, especially grid and non-grid spatial representations; subsequent whisker trimming had limited additional effects, but more clearly altered head-direction and border-cell tuning. In darkness with salient tactile landmarks, all spatially modulated cell types formed cue-anchored representations, and whisker trimming more strongly impaired grid and spatial coding. Some neurons remained stable after combined deprivation, consistent with support from boundary-related tactile signals. Additionally, a subset of MEC neurons showed activity correlated with whisker movement. These findings reveal flexible integration of visual and tactile information in MEC spatial coding.

Spatial navigation depends on the reliable integration of environmental reference cues from various sensory inputs, including visual[1], auditory[2,3], olfactory[4] and tactile stimuli[5], into internal spatial maps. While path integration[6–8]—computed from self-motion signals without the need for external references—forms a core component of spatial computation, external cues, particularly distal and proximal visual landmarks[8,9], are crucial for anchoring and calibrating internally generated estimates to improve navigational accuracy. The medial entorhinal cortex (MEC) plays a key role in this process by combining self-motion cues with external sensory information such as environmental boundaries and landmarks[10–12], thereby providing the hippocampus with a coherent framework for spatial cognition and memory.

The grid cell, initially characterized by Hafting et al. in 2005, constitutes the first identified spatially modulated cell type within the MEC[13], which exhibits action potentials at locations forming a hexagonal grid pattern. Alongside grid cells, the MEC encompasses other functionally distinct cell types, including head-direction (HD) cells[14], border cells[15,16], non-grid spatial cells[17] and speed cells[18,19]. It is hypothesized that grid cells play a dominant role in path integration, while HD cells and speed cells contribute to this process by likely providing self-motion-related information, as suggested by the continuous attractor model[12]. Additionally, border cells may help correct errors accumulated over time and distance in this process[11]. However, compared to grid cells, other spatially modulated cells in MEC sometimes

[1]State Key Laboratory of Membrane Biology, School of Life Sciences, Peking University, Beijing, China. [2]Peking University-International Data Group/McGovern Institute for Brain Research, Peking University, Beijing, China. [3]Peking-Tsinghua Center for Life Sciences, Academy for Advanced Interdisciplinary Studies, Beijing, China. [4]Peking University-Tsinghua University-National Institute of Biological Sciences Joint Graduate Program, Academy for Advanced Interdisciplinary Studies, Peking University, Beijing, China. [5]Chinese Institute for Brain Research, Beijing, China. [6]Peking University Chengdu Academy for Advanced Interdisciplinary Biotechnologies, Chengdu, China. e-mail: chenglin.miao@pku.edu.cn

exhibit different responses when the environment changes[17,20,21], which implies their respective sensitivity to external sensory input.

Although numerous studies have demonstrated how sensory inputs, particularly visual inputs, influence spatially modulated cells in MEC, such as HD cells[22,23] and grid cells[21,24], the specific role of tactile inputs in constructing a spatial cognitive map remains largely unexplored. Whiskers, also called facial vibrissae, are the primary tactile organs in rodents and their corresponding bilateral "whisking" behavior plays a crucial role in exploring environment[25]. Trimming animals' whiskers results in impaired performance in spatial learning tasks[26]. Previous studies have shown that the hippocampal CA1 region responds to whisker stimulation and is likely involved in the process of updating spatial cognitive maps[27]. Furthermore, the establishment of place fields in the hippocampus is modulated by tactile input, with different cells exhibiting varying response intensities[5]. These findings suggest that spatial maps can be constructed using tactile information, encompassing behaviorally relevant spatial elements such as object positions[28], specific boundaries[29,30], and environmental surfaces[31,32]. Strong evidence for this compensatory role comes from that tactile information plays a crucial compensatory role in the absence of visual information when rats are required to complete a gap crossing task in darkness[30]. Beyond the vibrissae, cutaneous mechanoreceptors distributed across other body surfaces—such as the glabrous skin of the plantar paws and the rhinarium—are represented in the rodent somatosensory system and participate in active exploratory behaviors[33,34]. However, whether and how the MEC responds to tactile inputs remain unclear.

In this study, we examined the alterations in spatial representation within the MEC following light deprivation and tactile deprivation using miniature two-photon microscopy. Our findings demonstrate that the MEC flexibly integrates available sensory inputs from the environment to construct spatial representations, with distinct functional cell types anchoring to external cues in a context-dependent manner and being modulated by both visual and tactile inputs. In a visual cue–dominated environment, darkness impaired the representations of all spatially modulated cell types; however, grid- and spatial-cell representations were more strongly affected by light deprivation than by subsequent whisker trimming in darkness. In contrast, in a dark tactile cue–dominated environment, all spatially modulated cell types anchored their firing to tactile landmarks and were more strongly altered by whisker trimming. When whisker trimming was combined with the removal of environmental walls in darkness, spatial representations across all cell types were severely degraded—most strikingly, the fields of border cells are nearly completely abolished. Furthermore, exploratory analyses revealed that a small subset of MEC neurons covaried with whisker movement, raising the possibility that whisker-related signals may be represented in MEC.

Results

Head-direction tuning in the MEC is reduced by darkness and whisker trimming

To investigate the influence of visual and tactile inputs on spatially modulated cells in the MEC, recombinant adeno-associated viruses (rAAVs) were used to express the Ca2+ indicators GCaMP6s and GCaMP6f in the MEC of mice (Supplementary Fig. 1). Using an autoregressive (AR) model-based algorithm to estimate the time constant, we found that the two calcium indicators, GCaMP6s and GCaMP6f, did not exhibit significant difference in calcium signal extraction performance in our data (Supplementary Fig. 2 a–c). A prism was implanted between the cortex and the cerebellum, enabling the acquisition of calcium signals via a miniature two-photon microscope[35] while the mice freely explored the open-field (Fig. 1a–d). Initially, the mice were allowed to freely explore an open field for approximately 30 minutes under illuminated conditions, establishing a stable baseline representation (Light, L). To assess the impact of visual deprivation, the lights were turned off and the mice were allowed to explore the same environment in complete darkness (Dark, D). Subsequently, their whiskers were trimmed and were reintroduced to the same environment, now deprived of both visual and tactile inputs (Dark/Whisker-trimmed, DW) (Fig. 1a). This design allowed us to evaluate the individual effects of light deprivation as well as the combined impact of darkness and whisker trimming, based on the premise that animals tend to rely on alternative sensory cues to support spatial cognition when a specific sensory modality is compromised[36,37]. A cohort of 13 male mice was used in this paradigm, and multiple types of spatially modulated neurons were identified within each field of view (FOV) (Supplementary Fig. 2d, e). All sessions were conducted in an open-field arena equipped with three distinct visual cue cards mounted on the surrounding walls (Environment 1).

First, we investigated the influence of visual and tactile inputs on head-direction tuning in the MEC. Calcium traces were extracted from 3,758 neurons, of which 406 (10.8%) were identified as HD cells from the baseline session and used for further analysis. HD cells were identified by comparing each neuron's real mean vector length (MVL) to a shuffle distribution generated by 1,000 circular time shifts of its calcium trace. A neuron was classified as an HD cell only if its observed MVL exceeded the 99th percentile of its shuffle distribution and its within-session tuning stability was greater than 0.5. In the baseline light session, the mean MVL of these HD cells was 0.52 (Supplementary Fig. 3a), with their preferred firing directions (PFDs) and the mice's head orientations being nearly uniformly distributed between 0 and 360° (Supplementary Fig. 3b, c). We subsequently calculated the tuning curves of selected HD cells for each experimental session and performed statistical analysis to compare the tuning abilities of the HD cell population. Our analysis revealed that both the MVL and head information (Head Info.) decreased across L, D, and DW sessions, indicating that HD tuning was reduced after light deprivation and further whisker trimming in darkness (Fig. 1e–j). Although many HD cells showed marked changes in tuning-curve shape and PFD after sensory deprivation, cell-centered local FOVs remained largely stable across the three sessions, arguing against unstable cell tracking as an explanation for these changes (Fig. 1k).

Individual HD cells exhibited heterogeneous responses to darkness or whisker trimming, with tuning strength and MVL showing varying degrees of change following sensory deprivation (Fig. 1k). To systematically assess the impact of sensory deprivation on HD cell tuning properties, we developed a subsampling-based approach to quantify whether individual HD cells exhibited statistically significant changes across three metrics: MVL change, PFD shift, and tuning curve correlation. For each pairwise session comparison, equal-duration data segments were randomly drawn from each session and this procedure was repeated 100 times; cells were classified as significantly affected if they showed a significant decline in MVL, a significant shift in PFD, or a significant reduction in cross-session tuning curve correlation relative to within-session stability (see Methods). Following the transition from light baseline to darkness, 167 of 406 (41.1%) HD cells exhibited a significant MVL decline, 122 of 406 (30.0%) cells showed a significant PFD shift, and 172 of 406 (42.4%) cells displayed a significant reduction in tuning curve correlation. We defined HD cells showing a significant change in at least one of these metrics as "affected cells," whereas cells showing no significant change in any metric were defined as "resistant cells." Based on this criterion, 257 of 406 (63.3%) HD cells were classified as affected cells, while 149 of 406 (36.7%) remained resistant to visual deprivation (Fig. 1l, upper). Following subsequent whisker trimming in darkness, 167 of 406 (41.1%) HD cells showed a significant MVL decline, 104 of 406 (25.6%) exhibited a significant PFD shift, and 110 of 406 (27.1%) showed a significant reduction in tuning curve correlation; 238 of 406 (58.6%) cells were classified as affected cells, while 168 of 406 (41.4%) remained resistant to whisker trimming (Fig. 1l, lower). The proportion of resistant cells was comparable

https://doi.org/10.1038/s41467-026-78000-2

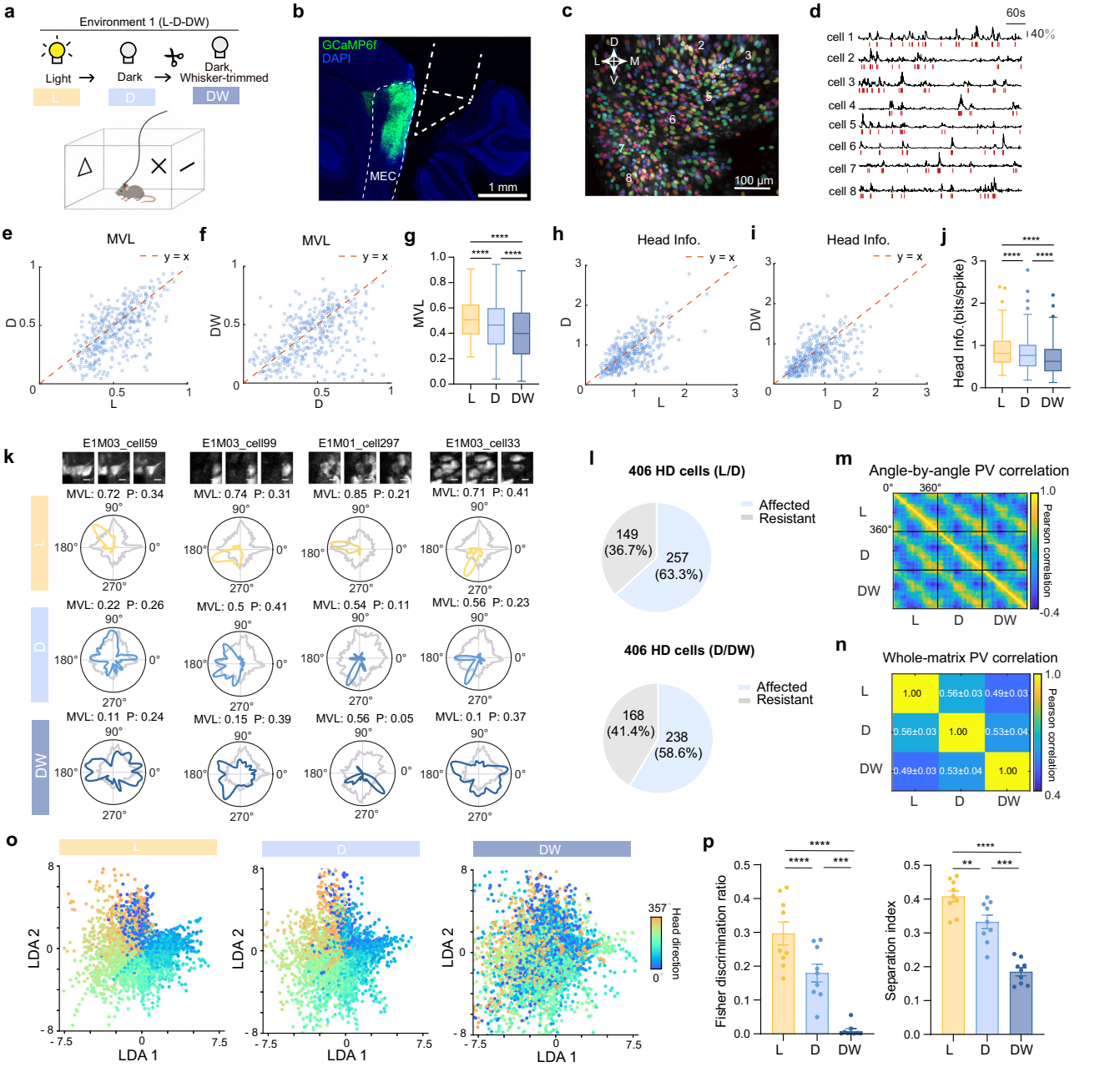


Fig. 1 | Light deprivation and whisker trimming reduce head-direction tuning. **a** Mice explored Environment 1 in light (L), darkness (D), and darkness after whisker trimming (DW). **b** Sagittal section showing GCaMP6f expression in the medial entorhinal cortex (MEC). Green, GCaMP6f; blue, DAPI; white dashed lines, MEC boundaries. Scale bar, 1 mm. **c** Representative field of view (FOV) showing Suite2p regions of interest (ROIs) in pseudocolors. Cells 1–8 correspond to (**d**). D, dorsal; V, ventral; M, medial; L, lateral. Scale bar, 100 µm. Panels (**b**) and (**c**) show representative images from one mouse; similar results were obtained in 37 mice. **d** Denoised ΔF/F traces from cells 1–8; red ticks indicate calcium events. Scale bars, 60 s and 40% ΔF/F. **e**–**g** Mean vector length (MVL) across sessions; scatter plots compare L versus D and D versus DW. **h**–**j** Corresponding analyses of head information. In (**g**, **j**), center lines, medians; boxes, 25th–75th percentiles; whiskers, values within 1.5 × the interquartile range; remaining points, outliers (repeated-measures one-way ANOVA with Geisser–Greenhouse correction followed by two-sided Tukey multiple-comparisons tests; $n = 406$ cells). **k** HD tuning curves with MVL and peak event rate (P); cell-centered FOV crops across L, D and DW are shown above. Scale bar, 10 µm. **l** Proportions of affected and resistant HD cells for L/D and D/DW. Affected cells changed in tuning-curve correlation, MVL and/or preferred firing direction; resistant cells changed in none. **m** Mean angle-by-angle population-vector (PV) correlation matrix across sessions. Each session spans 120 head-direction bins (0–360°). **n** Correlations between session-specific PV matrices for individual mice, mean ± SEM ($n = 13$ mice). **o** LDA projections of all-session HD-cell activity using an L-trained model, colored by head-direction angle. (p) Fisher discrimination ratio and separation index in mice with >20 HD cells. Dots indicate mice; bars show mean ± SEM (same tests; $n = 9$ mice). $^{****}P \le 0.0001$; $^{***}P \le 0.001$; $^{**}P \le 0.01$; $^{*}P \le 0.05$. See Supplementary Data 1 for exact P values and detailed statistics. Source data are provided as a Source Data file.

between the darkness and whisker-trimming conditions (36.7% vs. 41.4%; $\chi^2 = 1.9$, $P = 0.17$), indicating that the two manipulations produced similar fractions of unaffected HD cells.

We next assessed population-level HD coding across consecutive sessions. Angle-by-angle PV correlations were calculated across 120 head-direction bins and visualized as cross-session correlation matrices (Fig. 1m). Correlations between the complete population tuning

matrices indicated reduced cross-session stability following darkness and subsequent whisker trimming (Fig. 1n; $n = 13$ mice, mean ± SEM: L/D: 0.56 ± 0.03; D/DW: 0.49 ± 0.03). To further examine changes in HD encoding ability, we applied linear discriminant analysis (LDA) to reduce the dimensionality of neural activity recorded from the HD cell population. In the light condition, neural representations of different head-direction angles were well-separated, demonstrating accurate HD tuning under normal sensory conditions (Fig. 1o and Supplementary Fig. 3f). This representation remained stable across time within the baseline session, as evidenced by the consistent separation of head directions when projecting neural activity from the first and second halves of the session separately (Supplementary Fig. 3d). In the dark condition, the separation between head directions was notably reduced, suggesting a drift in population-level HD representation away from that established under illuminated conditions, likely due to the absence of visual cues. Following subsequent whisker trimming in darkness, the separation of head-direction representations was further reduced in some mice (Fig. 1o and Supplementary Fig. 3f). Quantitative analysis further confirmed these effects, since both the Fisher's discrimination ratio and the separation index exhibited a significant decline from the light condition to the dark and further to the dark with whisker trimming conditions (Fig. 1p). These metrics indicate a progressive drift in the original population-level HD representation, with the most pronounced impairment occurring under combined visual and whisker-mediated tactile deprivation. Nevertheless, when we applied LDA to the DW session and used it as the reference for dimensionality reduction, we found that the HD neural population still retained some capacity to distinguish head direction angles (Supplementary Fig. 3e), although the discriminability was reduced compared with the baseline light session. Thus, while sensory deprivation reduced the fidelity of HD tuning, the directional signal was not completely abolished.

Following the DW session, we reintroduced visual input by turning the lights back on and allowed the animals to freely re-explore the environment (Light/Whisker-trimmed, LW; Supplementary Fig. 3g). However, the population-level HD tuning strength did not recover (Supplementary Fig. 3h), indicating that the effects of whisker trimming persisted despite restoration of visual cues. At the single-cell level, HD responses exhibited substantial heterogeneity. In some cells, MVL increased and a clear PFD re-emerged (Supplementary Fig. 3i), whereas others failed to recover, potentially reflecting differential dependence on sensory inputs. When LDA was applied again to evaluate population-level encoding of head direction, considerable variability was observed across mice (Supplementary Fig. 3j). In some animals, the altered HD representation did not recover during the subsequent LW session (Supplementary Fig. 3j), indicating that reintroduction of visual cues alone was insufficient to restore the original HD representation. However, when LDA was trained and projected using data from the LW session itself, the population activity appeared to encode head direction more effectively than when baseline light-session activity was used as the reference (Supplementary Fig. 3j). This finding suggests that, following reintroduction of visual input, the HD network may have stabilized to a new, internally consistent reference frame rather than returning to the original alignment.

In addition, the accuracy of DLC in tracking animals' position and the quality of the imaging data were consistent across all sessions, thereby ruling out the possibility that the observed changes in cells' firing patterns were due to these factors (Supplementary Fig. 4a–c). General locomotor and exploratory behavior also remained largely unaffected following whisker trimming (Supplementary Fig. 4d). Animals maintained extensive spatial coverage of the arena throughout all sessions (Supplementary Fig. 4e), and no significant differences were observed in running speed, time spent near the boundaries, or wall-directed exploratory behavior after whisker trimming (Supplementary Fig. 4f–h). Notably, however, whisker trimming resulted in a significant reduction in head angular speed (Supplementary Fig. 4i). Given that whiskers contribute to head orientation, their removal may influence head movement dynamics in addition to reducing tactile input. Therefore, we cannot exclude the possibility that changes in angular head velocity-related signals contributed to the disruption of HD tuning, as vestibular/AHV inputs are known to influence HD circuits[38,39].

Importantly, we subjected three additional mice to the same experimental paradigm but without whisker trimming, to serve as control experiments (Supplementary Fig. 5a, b). The results showed that MVL and head information of HD cells decreased after light deprivation. However, no further changes were observed during a subsequent dark session. These findings suggest that the deterioration in HD tuning after whisker-trimming was not due to a progressive drift in cellular representations during darkness, but rather caused by the deprivation of tactile cues provided by the whiskers. Notably, similar patterns were observed in other types of spatially modulated cells (Supplementary Fig. 5).

Light deprivation and whisker trimming modestly alter border-cell representations

In addition to HD cells, MEC contains various types of spatially modulated cells, including border cells, grid cells and non-grid spatial cells. We next sought to determine whether border cells in MEC are influenced by visual inputs and whisker-mediated tactile inputs. A total of 223 neurons (5.9%) were identified as border cells (see Methods), with an average border score of 0.63 (Supplementary Fig. 6a).

Our analysis revealed that the maintenance of boundary fields is supported by both visual and tactile inputs. Specifically, both border score and spatial information were reduced in darkness relative to the light condition (Fig. 2a–f). Further whisker trimming in darkness did not cause an additional decrease in border score, but selectively reduced spatial information, indicating a limited additional effect on border-cell spatial coding after visual deprivation (Fig. 2a–h). The disrupted firing pattern of the border cell population was not observed in the control experiments (Supplementary Fig. 5a, c). Following disruption of sensory input, border cells exhibited markedly increased firing in non-border regions, and a subset lost border-selective tuning entirely after whisker trimming (Fig. 2g).

To quantify the extent to which visual and whisker-mediated tactile deprivation impaired border cells, we applied an approach analogous to that used for HD cells, assessing three complementary metrics: the border score, the spatial precision of border firing fields (measured as the distance from the peak firing location to the nearest wall), and the stability of the spatial firing pattern across sessions (see Methods). Under dark conditions, 131 of 223 border cells (58.7%) showed a significant reduction in border score relative to the baseline session; 56 of 223 cells (25.1%) exhibited a significant increase in peak firing distance to the nearest wall; and 85 of 223 cells (38.1%) showed a significant reduction in cross-session rate map correlation (L/D) relative to their within-session correlation of baseline session (L). When the three metrics were considered jointly, 162 of 223 border cells (72.6%) showed a significant change in at least one metric and were therefore defined as affected cells, whereas only 61 of 223 border cells (27.4%) showed no significant change in any metric and were defined as resistant cells (Fig. 2h, upper). Following additional whisker trimming under dark conditions, 100 of 223 border cells (44.8%) showed a significant reduction in border score; 67 of 223 cells (30.0%) displayed a significant increase in peak-to-wall distance; and 83 of 223 cells (37.2%) showed a significant reduction in cross-session rate map correlation (D/DW) relative to within-session correlation of dark session (D). 146 of 223 border cells (65.5%) were classified as affected cells, whereas 77 of 223 border cells (34.5%) remained resistant and stably maintained their previous firing patterns (Fig. 2h, lower). No significant difference was found in the proportion of border cells unaffected by darkness versus

https://doi.org/10.1038/s41467-026-78000-2

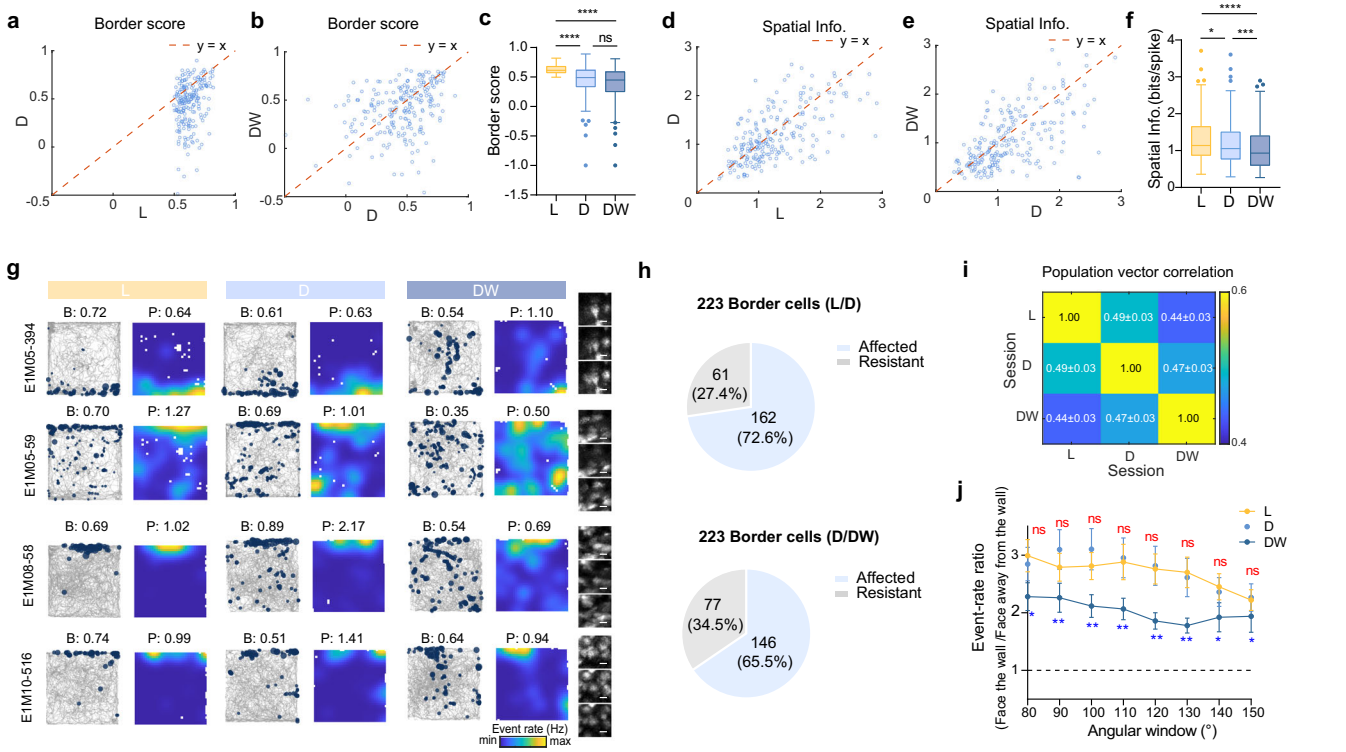


Fig. 2 | Light deprivation and whisker trimming modestly alter border-cell representations in MEC. a Scatter plot comparing border scores of all border cells between light (L) and darkness (D). **b** Scatter plot comparing border scores between D and darkness after whisker trimming (DW). Dashed lines indicate y = x. **c** Box plot showing that border scores decreased from L to D and remained lower in DW. **d**–**f** Corresponding analyses of spatial information after light deprivation and subsequent whisker trimming. In (**c**, **f**), center lines indicate medians, boxes the 25th–75th percentiles, and Tukey whiskers the most extreme values within 1.5 × the interquartile range; values beyond the whiskers are plotted individually (repeated-measures one-way ANOVA with Geisser–Greenhouse correction followed by two-sided Tukey multiple-comparisons tests; n = 223 border cells from 13 mice).**g** Representative trajectories and rate maps of border cells across L, D and DW. Trajectories are shown in gray and calcium events in dark blue; map color indicates event rate. B and P indicate border score and peak event rate. Corresponding cell-centered FOV crops from the three sessions are shown on the right. Scale bar, 10 µm. **h** Proportions of affected and resistant border cells after light deprivation (L/D) or whisker deprivation (D/DW). Affected cells changed significantly in rate-map correlation, border score and/or distance of the peak field from the nearest boundary; resistant cells did not. **i** Population-vector correlations across L, D and DW, averaged across mice and shown as mean ± SEM (n = 13 mice). **j** Wall-facing modulation, quantified as the calcium-event-rate ratio when mice faced toward versus away from the wall within boundary regions, evaluated across angle limits using all cells with valid measurements (n = 223 border from 13 mice). Values are mean ± SEM; the dashed line indicates a ratio of 1. Red annotations indicate pairwise L–D comparisons and blue annotations pairwise D–DW comparisons using multiple unpaired t-tests. ****$P \le 0.0001$; ***$P \le 0.001$; **$P \le 0.01$; *$P \le 0.05$; ns, $P > 0.05$. See Supplementary Data 1 for exact P values and detailed statistical information. Source data are provided as a Source Data file.

whisker trimming (Chi-square test, $\chi^2 = 1.6$, $P = 0.10$). The population vector of the border-cell firing patterns was also altered following light deprivation and subsequent whisker trimming (Fig. 2i).

Because some border cells also exhibited head-direction tuning (38 of 223, 17.0%), we repeated the analysis in pure border cells after excluding these cells. Pure border cells showed similar responses to light deprivation and subsequent whisker trimming, indicating that the border-cell effects were not driven by conjunctive head-direction tuning (Supplementary Fig. 6b). The presence of border cells in our recordings was validated by the emergence of new firing fields in a subset of cells when a wall was inserted into the environment one day prior to the whisker-trimming experiments for some mice (Supplementary Fig. 6d). Cross-day comparisons further demonstrated that, among the border cells responsive to the newly inserted wall, some maintained stable firing properties across sensory conditions, while others were affected by darkness and whisker trimming (Supplementary Fig. 6e). Border score and spatial information did not improve during the final LW session, indicating that the degraded spatial coding of border cells was not restored after only visual inputs were reintroduced (Supplementary Fig. 6c).

Unlike HD cells and grid cells, border cells have not been shown to possess an attractor network structure that could autonomously maintain representations. Consequently, border cells likely depend mostly on external sensory input to establish and sustain boundary representations—whether through direct visual observation of the enclosure walls or through physical contact mediated by the whiskers or snout. To examine wall-facing modulation of border-cell activity, we analyzed calcium-event rates when animals were located within the boundary zone and faced either toward or away from the wall. For each angular window, we calculated a wall-facing event-rate ratio, defined as the calcium-event rate during wall-facing epochs divided by that during wall-away epochs (Supplementary Fig. 6 f; see Methods). Thus, a ratio greater than 1 indicates stronger border-cell activity when the animal faced the wall. Border cells showed a wall-facing preference across sessions (Supplementary Fig. 6g). This preference was not detectably altered by darkness but was reduced after whisker trimming, although the ratio remained above 1, indicating residual wall-facing modulation even under combined sensory deprivation (Fig. 2j). Together, the persistence of wall-facing preference, the modest effect on border score, and the maintenance of boundary-specific firing in some border cells suggest that additional sensory inputs—such as direct physical contact of the snout or body with the wall—may also contribute to border-cell activation at environmental boundaries.

Darkness alters grid-cell spatial coding with limited additional effects of subsequent whisker trimming in a visual cue–dominated environment

Grid cells are the predominant type of spatially modulated cells in the MEC and have long been regarded as implicated in path integration[12,40]. Historically, grid cells were thought to operate independently of external sensory inputs, generating their characteristic hexagonal firing patterns based solely on self-motion information. However, recent studies have challenged this notion, demonstrating that spatial coding performance of grid cells is modulated by various sensory inputs, especially by visual cues[10,21].

In our study, we identified 215 grid cells (5.7% of all recorded neurons), with an average grid score of 0.65 (Supplementary Fig. 7a). We observed that the overall grid score significantly decreased in darkness, consistent with previous findings[21], whereas spatial information remained largely unchanged across sessions (Fig. 3a, c, d and f). Further whisker trimming in darkness did not produce an additional decrease in either grid score or spatial information (Fig. 3b, c, e and f), suggesting a small influence of interactive effects of visual and tactile deprivation on grid cell function. Many grid cells lost their characteristic hexagonal firing patterns in darkness but showed no further deterioration following whisker trimming (Fig. 3g). Given recent evidence that grid cells are anatomically clustered[41], we selected four mice with enriched grid cells in the imaging FOV (> 20 grid cells per animal) and performed statistical analyses exclusively on grid cells from these animals to minimize the potential confound of false-positive grid cell inclusion. Consistent with the full dataset, grid cells from these four mice showed substantial degradation of spatial coding under visual deprivation, with no significant further decline following whisker trimming (Supplementary Fig. 7b, c). Conjunctive grid × HD cells and grid cells without directional tuning also exhibited similar patterns of sensory dependence (Supplementary Fig. 7d, e).

Following light deprivation, 143 of 215 grid cells (66.5%) exhibited a significant reduction in grid score relative to the baseline light session; 59 of 215 cells (27.4%) showed a significant shift in peak firing location; and 97 of 215 cells (45.1%) displayed a significant decrease in cross-session rate map correlation relative to within-session baseline. When all three metrics were considered jointly, 181 of 215 grid cells (84.2%) were classified as affected cells after light deprivation, whereas 34 of 215 cells (15.8%) remained resistant, showing no significant change in any metric (Fig. 3h, upper). Following subsequent whisker trimming under dark conditions, 82 of 215 cells (38.1%) were unaffected across all three metrics (Fig. 3h, lower)—a proportion significantly greater than that observed under darkness alone (Chi-square test, $\chi^2 = 27.2$, $P = 1.8 \times 10^{-7}$).

To further validate these findings, we conducted a detailed examination of the firing maps of each grid cell (see Methods). The analysis revealed that the mean field size of grid cells became larger in darkness (Fig. 3i), suggesting a potential expansion of grid fields. This change was accompanied by an increase in both the standard deviation of grid spacing (Fig. 3j) and ellipticity (Fig. 3k), indicating that grid patterns became less regular in darkness. However, these parameters did not show further deterioration after subsequent whisker trimming (Fig. 3i–k). Instead, some measures, such as grid-spacing variability and ellipticity, tended to shift back toward baseline levels in the DW session. This partial recovery may reflect increased experience or familiarity with the dark environment.

Additionally, we decoded position based on the population activity of four mice that possessed more than 20 grid cells and compared their decoding performance to baseline conditions after sensory deprivation. Specifically, we split the baseline light session into two halves. The first half served as the training set, while the second half—along with the second halves of other sessions—was used to construct the test set for each experimental condition. The decoding performance improved as the number of participating grid cells increased (Supplementary Fig. 7f). Because the number of mice with grid cell–enriched FOVs was limited, position decoding based only on grid cells was not sufficiently accurate. The decoding error was significantly lower than the shuffled control only under the light condition (Supplementary Fig. 7f). Since grid cells are not the only contributors to spatial localization and the decoding results based solely on grid cells were not precise enough, we next included all functional cell types in the position decoder to assess the impact of darkness and further whisker trimming on the animals' spatial coding ability. MAE was significantly lower during the baseline light sessions compared to shuffled controls (Fig. 3l, m; see Methods). In darkness, the MAE increased compared to the light environment but remained unchanged after whisker trimming (Fig. 3l). This suggests that, in this case, population-level spatial decoding was altered after light deprivation but showed no detectable additional change after subsequent whisker trimming in darkness. Notably, despite the sensory deprivation, the decoder across all sessions consistently produced a lower MAE than the shuffled results (Fig. 3l), indicating that animals retain some ability to construct a cognitive map of the environment even in the absence of visual and whisker-mediated tactile inputs, potentially through path integration. At the population level, grid scores and spatial information did not recover after re-exposure to the light condition (Supplementary Fig. 7g). However, a subset of grid cells exhibited more regular rate maps and increased grid scores, indicating pronounced heterogeneity within the population (Supplementary Fig. 7h). Because light deprivation preceded whisker trimming in this paradigm, whisker trimming in darkness was not an independent manipulation, and the DW session represented the combined effects of visual deprivation and subsequent removal of whisker-mediated tactile input. Thus, the limited additional effect of whisker trimming at the population level may partly reflect reduced sensitivity of grid cells to further sensory deprivation after visual input had already been removed. Nevertheless, individual-cell analyses showed that a considerable fraction of grid cells was still affected by whisker trimming (Fig. 3h).

Non-grid spatial cells exhibited response patterns comparable to those of grid cells. Among the 3756 recorded cells, 501 were identified as non-grid spatial cells, with a mean spatial information of 1.26. Although their spatial coding was significantly disrupted in darkness, it was not further impaired by subsequent whisker trimming (Supplementary Fig. 8a). In addition, the mean field size of spatial cells increased significantly in darkness (Supplementary Fig. 8b). 405 of 501 spatial cells (80.8%) showed a significant change in at least one metric after light deprivation and were classified as affected cells, whereas 96 of 501 cells (19.2%) showed no significant change in any metric and were classified as resistant cells (Supplementary Fig. 8c, upper). Following additional whisker trimming in darkness, 275 of 501 spatial cells (54.9%) were classified as affected cells, while 226 of 501 cells (45.1%) remained resistant, indicating that further whisker trimming had a more limited additional effect on non-grid spatial cells after light deprivation (Supplementary Fig. 8c, lower). Most spatial cells displayed increased out-of-field firing after light deprivation, which did not worsen following whisker trimming (Supplementary Fig. 8d). Notably, similar to what we observed in grid cells, a small subset of cells appeared to show slightly more precise spatial representations after whisker trimming, possibly reflecting increased familiarity with the dark environment (Supplementary Fig. 8d).

All spatially modulated cell types can anchor to tactile cues when tactile input dominates

Although grid scores of grid cells and spatial information of spatial cells did not significantly decline at the population level following whisker trimming (Fig. 3c and Supplementary Fig. 8a), and the accuracy of position decoding from neural activity was not further impaired in darkness (Fig. 3l), a substantial subset of grid cells and

https://doi.org/10.1038/s41467-026-78000-2

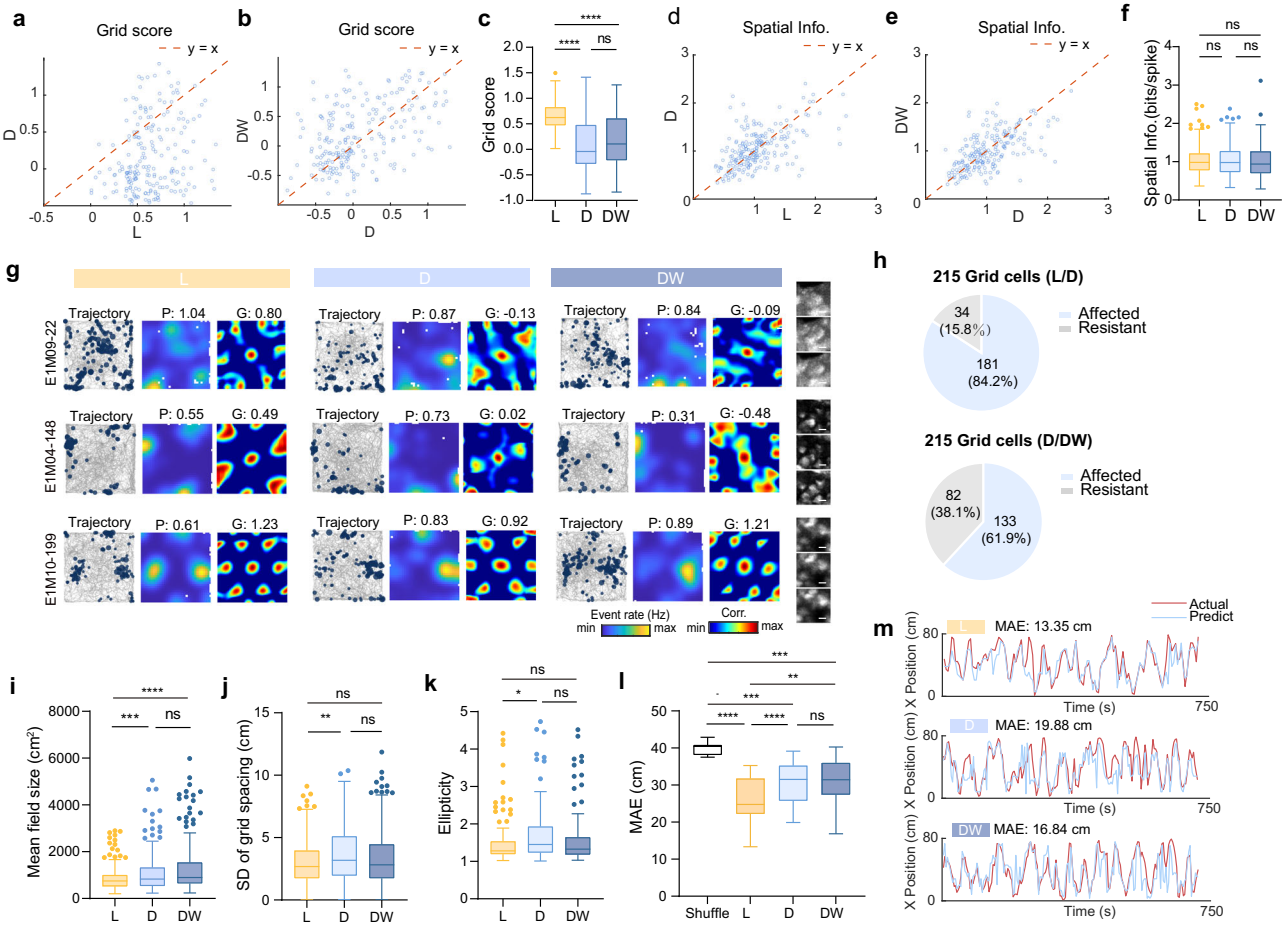


Fig. 3 | Darkness alters grid-cell spatial coding with limited additional effects of subsequent whisker trimming in a visual cue–dominated environment. **a**, **b** Scatter plots comparing grid scores between light (L) and darkness (D), and between D and darkness after whisker trimming (DW), respectively. Dashed lines indicate y = x. **c** Box plot showing reduced grid scores after light deprivation, with no further decrease from D to DW (repeated-measures one-way ANOVA followed by two-sided Tukey multiple-comparisons tests; $n = 215$ grid cells from 13 mice). **d**–**f** Spatial-information analyses showing no significant differences across sessions (same tests and n). In (**c**, **f**, **i**–**l**), center lines are medians, boxes show the 25th–75th percentiles, and Tukey whiskers extend to the most extreme values within 1.5 × the interquartile range; values beyond the whiskers are plotted individually. **g** Representative examples of color-coded rate maps and corresponding auto-correlograms for grid cells across different sessions. Grid score (G) and peak rate (P) are indicated. Cell-centered FOV crops from L, D and DW are shown on the right. Scale bar, 10 µm. **h** Proportions of affected and resistant grid cells for L/D and D/DW comparisons. Affected cells changed in rate-map correlation, grid score and/or peak firing-location shift; resistant cells did not. **i**–**k** Box plot showing changes of mean grid-field size, standard deviation (SD) of grid spacing and grid ellipticity across sessions (repeated-measures one-way ANOVA followed by two-sided Tukey multiple-comparisons tests; (**i**) 199 pairs; (**j**) 179 pairs; (**k**) 131 pairs). **l** Mean absolute error (MAE) of position decoded from all spatially modulated cells across different conditions. MAE remained below shuffle in all sessions and increased from L to D, with no further increase from D to DW (same tests; $n = 13$ mice). **m** Actual (red) and decoded (blue) x-positions across L, D and DW in one mouse; MAE is shown for each session. $^{****}P \le 0.0001$; $^{***}P \le 0.001$; $^{**}P \le 0.01$; $^{*}P \le 0.05$; ns, $P > 0.05$. See Supplementary Data 1 for exact P values and detailed statistical information. Source data are provided as a Source Data file.

spatial cells nonetheless exhibited significant changes in individual metrics after whisker deprivation (Fig. 3h and Supplementary Fig. 8c). Moreover, the reintroduction of light failed to restore population-level grid scores and spatial information (Supplementary Fig. 7g), suggesting that whisker-mediated tactile deprivation did exert effects on some neurons. However, given that spatial representations in this experiment were established under light conditions with prominent visual cue cards (Environment 1, E1; Fig. 1a), while the tactile cues present in the environment were comparatively subtle (e.g., minor textural variations and surface irregularities on the floor and walls of the paper-lined arena), the impact of whisker deprivation on grid and spatial cells was considerably more limited than that of light deprivation, possibly because whisker-mediated tactile input in this environment mainly contributed to the animals' perception of environmental boundaries. In addition, because visual deprivation was introduced before whisker trimming in Environment 1, the effects of darkness may have partially obscured additional contributions of whisker-mediated tactile input.

In naturalistic settings, rodents navigate environments of far greater complexity, characterized by objects of diverse materials, irregular terrain, and boundary structures with varied surface properties, often under conditions of dim ambient illumination. Under such circumstances, tactile input likely plays a role comparable to that of visual cues in supporting spatial orientation. To directly examine whether tactile cues can anchor spatial representations in the absence of visual information, we designed a new open-field arena rich in salient, polarizing tactile landmarks (Environment 2, E2). Two strips of sandpaper with distinct grit sizes were affixed to two walls of the arena, and an additional square piece of sandpaper was placed on the floor in one corner (Fig. 4a, top). No visual cue cards were introduced, and the animals explored the arena in complete darkness throughout the training period. After approximately one week of habituation, we used this tactile cue–dominated environment to examine whether different types of cells were modulated by environmental tactile cues.

https://doi.org/10.1038/s41467-026-78000-2

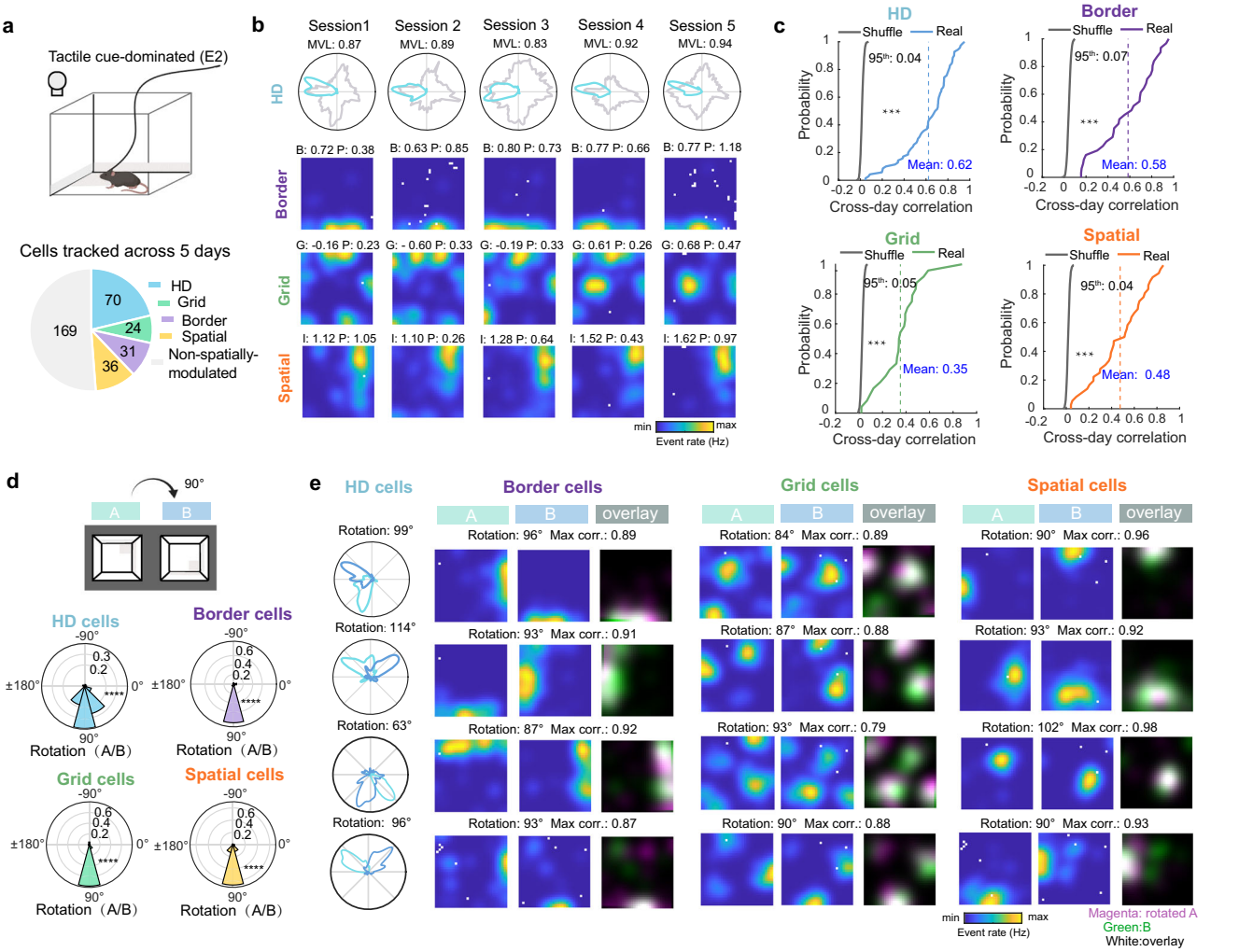


Fig. 4 | MEC spatial representations can anchor to tactile cues in darkness. **a** Schematic of the tactile cue–dominated environment (Environment 2, E2). Mice explored an open-field arena in darkness without visual cue cards. Sandpaper cues of different grit sizes were attached to the floor and two walls. Bottom, numbers of HD, border, grid, spatial and non-spatially modulated cells tracked across five days. **b** Representative tuning curves across days in darkness. From top to bottom: HD, border, grid and spatial cells. MVL, border score (B), grid score (G), spatial information (I) and peak event rate (P) are indicated. **c** Cross-day stability, quantified as the mean pairwise correlation of tuning curves or rate maps across five sessions. Observed correlations were compared with null distributions generated by independently permuting cell identities across sessions (1,000 shuffles; one-sided permutation test). Stability exceeded shuffle for all four cell types (P = 0.001). Black and colored curves show shuffle and real distributions. Black dashed lines and values indicate the 95th percentiles of shuffle distributions; colored dashed lines and values indicate mean real correlations. **d** Rotation of tactile cues and neural representations. After representations were established in session A, all tactile cues were rotated 90° clockwise before session B. Polar plots show rotation-angle distributions. HD cells: n = 107, circular mean = 83.7°, Rayleigh test, Z = 65.9, $P = 8.8 \times 10^{-28}$; border cells: $n = 80$, circular mean = 86.6°, Z = 60.57, $P = 2.3 \times 10^{-25}$; grid cells: n = 62, circular mean = 90.3°, Z = 36.0, $P = 1.6 \times 10^{-15}$; spatial cells: $n = 180$, circular mean = 88.9°, Z = 143.3, $P = 2.1 \times 10^{-60}$. **e** Representative tuning curves or rate maps from sessions A and B. HD curves are shown in light green and blue. For border, grid and spatial cells, each row shows maps from A and B and their overlay. White indicates overlap between the optimally rotated session-A map (magenta) and session-B map (green). $^{****}P \le 0.0001$; $^{***}P \le 0.001$; $^{**}P \le 0.01$; $^{*}P \le 0.05$; ns, $P > 0.05$.

We first asked whether animals could establish stable spatial representations across days in this tactile cue–dominated environment in the absence of visual cues. After habituation, we performed calcium imaging across five recording days in three mice (Supplementary Fig. 9a). Spatially modulated cells were identified from the last recording day (Fig. 4a, bottom), and their tuning curves or rate maps remained similar across days (Fig. 4b). To quantify cross-day stability, we calculated the mean pairwise correlation of each cell's tuning curves or rate maps across the five sessions and compared it with shuffled controls generated by independently permuting cell identities within each recording day. The cross-day correlations of all four classes of spatially modulated cells were significantly higher than the shuffle levels, indicating that MEC neurons can maintain stable spatial representations across days in a dark, tactile cue–dominated environment (Fig. 4c).

Moreover, we conducted a cue-rotation experiment to assess whether spatial representations rotated coherently with the tactile cues (Fig. 4d, top). After mice established stable spatial representations in the initial configuration (Session A), the arena was carefully cleaned and the entire environment—including the sandpaper landmarks along with residual subtle tactile features on the walls and floor—was rotated 90° clockwise (Session B), and neural tuning curves were re-acquired. To quantify the alignment between sessions, each cell's tuning curve from Session A was rotated in 3° increments and correlated with the corresponding Session B tuning curve across all rotation angles, generating a rotation-correlation profile. The correlation peaked robustly at 90° clockwise rotation for nearly all recorded cells

and spatial representations in all 6 mice underwent coherent rotation (Supplementary Fig. 9b). We defined the rotation angle as the angular offset at which the correlation between the rotated Session A and Session B tuning curves was maximized. The rotation angles of HD cells, border cells, grid cells, and spatial cells were all significantly clustered around 90° (Fig. 4d, bottom), consistent with the rotation of the tactile cues. Representative examples are illustrated in Fig. 4e, demonstrating that individual neurons' spatial representations from Session A, upon 90° rotation, closely matched those recorded in Session B. Collectively, these results demonstrate that in a visually deprived, completely dark environment, all classes of spatially modulated cells in the MEC can anchor to environmental tactile cues.

Although grid and spatial cells could form relatively stable spatial representations in the dark tactile cue–dominated environment and their rate maps rotated coherently with tactile cues, their cross-day stability was lower than that of HD and border cells (Fig. 4c). We therefore compared these results with five-day recordings from an independent cohort of three mice in Environment 1, a visual cue–dominated arena, after one week of habituation. Cells in this lighted environment also showed stable spatial representations across days (Supplementary Fig. 10a). Using the same analysis, we found that HD and border cells showed comparable cross-day stability between the two environments, whereas grid and spatial cells were more stable in the visual cue–dominated environment (Supplementary Fig. 10b). Thus, grid and spatial cells can form tactile cue–anchored representations in darkness, but their long-term stability appears greater when visual cues are available.

Whisker trimming disrupts tuning of all types of spatially modulated cells in a tactile cue–dominated environment

Given that various spatially modulated cells can anchor their firing to tactile cues in Environment 2 (Fig. 4), whiskers—as the primary tactile sensory organs in rodents—likely play an important role in this process. We therefore hypothesized that whisker trimming would exert a more pronounced impact on grid cells and other spatially modulated cells under these conditions compared to Environment 1 (Figs. 1–3). To test this, we recorded MEC neuronal activity across 12 FOVs from 10 additional male mice and examined the effects of whisker trimming (Supplementary Fig. 11a). Whisker trimming did not produce any overt behavioral abnormalities (Supplementary Fig. 11b–e).

Consistent with observations in Experiment 1, tuning of HD cells and border cells was significantly disrupted following whisker deprivation, as evidenced by marked reductions in tuning strength and firing specificity of individual cells (Supplementary Fig. 11f–k). In contrast to Environment 1, however, grid scores of grid cells also declined significantly after whisker trimming in Environment 2 (Fig. 5a), though spatial information remained unchanged (Fig. 5b). Moreover, grid cell properties that were unaffected by whisker trimming in Environment 1—including mean field size, standard deviation of grid spacing, and ellipticity—all showed significant changes in Environment 2 (Fig. 5c–e), indicating that the regularity of grid cell firing patterns was substantially degraded. Of the 164 grid cells recorded, only 29 (17.7%) exhibited no detectable change after whisker trimming across all metrics, whereas the remaining cells showed a significant change in at least one metric, including grid score reduction, rate-map reorganization, or peak firing location shift (Fig. 5f). Similarly, the spatial representations of spatial cells showed a marked loss of spatial selectivity after whisker deprivation (Fig. 5g). Only 24.5% of spatial cells remained entirely unaffected in spatial information, rate map correlation, and peak firing location (Fig. 5h). The position decoder trained on neuronal activity of all spatially modulated cells from the dark baseline session (D) showed a significant decrease in decoding accuracy following whisker trimming (DW), confirming that the loss of whisker-mediated tactile input under these conditions impaired the fidelity of animals' spatial coding ability (Fig. 5i–j). At the single-cell level, the rate maps of the majority of grid cells and spatial cells underwent pronounced alterations: some grid cells entirely lost their characteristic hexagonal firing patterns (Fig. 5k), and some spatial cells showed complete abolition of spatial selectivity (Fig. 5l).

In this experiment, two mice underwent a second round of whisker trimming after their whiskers had regrown to sufficient length following the initial deprivation. During the second manipulation, neural activity was recorded from newly imaged fields of view. Notably, repeated whisker trimming produced effects on spatially modulated cells that were comparable in magnitude to those observed after the first trimming (Supplementary Fig. 11 l). The reproducibility of these effects argues against the possibility that the observed degradation in spatial representations was driven by transient behavioral abnormalities, stress responses, or incomplete task adaptation.

Spatial representations anchored to tactile cues are preferentially disrupted by whisker trimming

As Environment 2 provides rich tactile but no visual cues, spatially modulated cells there are expected to rely predominantly on whisker-mediated input for spatial coding, predicting greater disruption from whisker trimming than in Environment 1. Consistent with this, the proportion of whisker deprivation-resistant cells (defined as those showing no significant change in any spatial metric following trimming) was significantly lower in Environment 2 than in Environment 1 for HD cells, grid cells, and spatial cells (Fig. 5m). This finding further suggests that the effects of whisker trimming cannot be solely attributed to trimming-induced alterations in locomotor behavior or arousal state. Border cells were the exception, showing no significant difference between environments (Fig. 5m), likely because they mainly rely on whisker-mediated boundary sensing regardless of the broader tactile context.

Rodents rely on their whiskers to detect surface textures. In our arena, the sandpaper patch positioned in the upper-right corner provided the dominant tactile cue apart from the enclosing walls. This cue could therefore serve either as a local tactile landmark directly anchoring the firing fields of spatially modulated cells or as a stable reference to correct errors accumulated during path integration. We thus hypothesized that whisker trimming would preferentially disrupt firing patterns within the sandpaper region-of-interest (ROI) relative to the rest of the arena. To test this hypothesis, we first computed population-averaged rate maps for each of the four spatially modulated cell types by averaging event rates across all cells of a given type within each spatial bin (Fig. 6a–d). HD cells and border cells showed no pronounced reduction in mean firing rate within the ROI following whisker trimming, consistent with the fact that HD cell activity is basically independent of spatial location and border cell firing is primarily constrained to environmental boundaries. In contrast, grid cells and spatial cells exhibited a prominent reduction in population mean rate within the ROI (Fig. 6c, d). We next examined whether whisker trimming preferentially affected cells whose spatial representations depended on tactile information from the ROI. Grid cells were classified as ROI cells if at least one grid field was located within the ROI, and as non-ROI cells otherwise (see Methods), yielding 44 ROI grid cells and 120 non-ROI grid cells (Fig. 6e). Grid scores decreased significantly in both groups after whisker trimming and the magnitude of reduction did not differ between ROI and non-ROI grid cells (Fig. 6f). However, field-level analysis revealed a selective effect: grid fields located within the ROI (ROI fields) were significantly more likely to disappear following whisker trimming than non-ROI fields (Fig. 6g, h, see Methods). A field was classified as lost if no corresponding field was detected in the subsequent session or if its spatial overlap with the original field was less than 20%. We performed a parallel analysis for spatial cells. Based on the location of the primary field, defined as the largest spatial field, 52 cells were classified as ROI spatial cells and 561 as non-ROI spatial cells (Fig. 6i, see Methods). ROI spatial cells exhibited a

https://doi.org/10.1038/s41467-026-78000-2

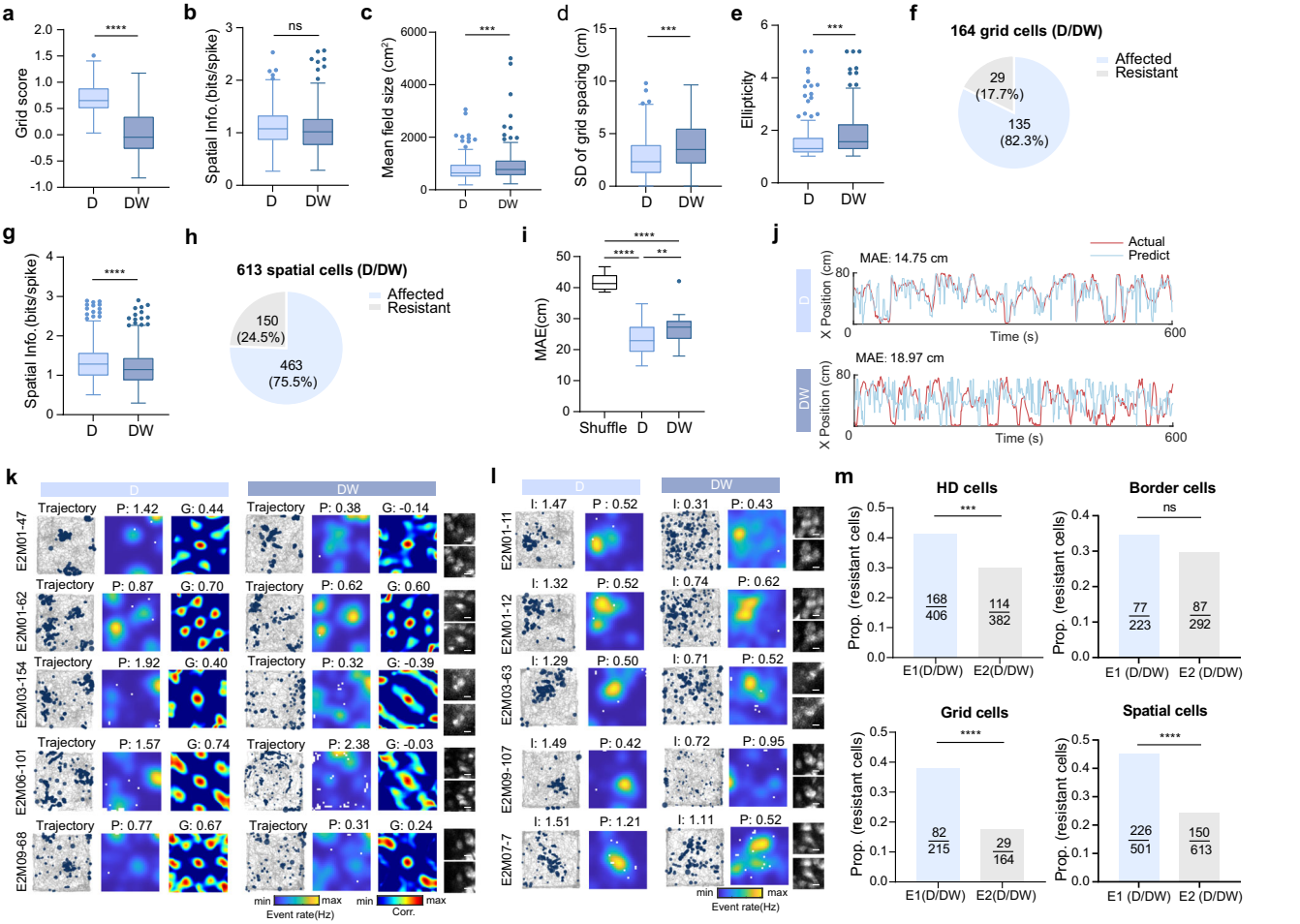


Fig. 5 | Whisker trimming more strongly alters grid- and spatial-cell representations in a tactile cue–dominated environment. a–**e** Box plots comparing grid score, spatial information of grid cells, mean grid-field size, SD of grid spacing and grid ellipticity between darkness (D) and darkness after whisker trimming (DW). Trimming reduced grid score and increased field size, spacing variability and ellipticity, without changing spatial information (two-sided Wilcoxon signed-rank tests; (a, **b**) n = 164 grid cells, (**c**, **d**) n = 154 pairs, (**e**) n = 130 pairs). **f** Affected and resistant grid-cell proportions after whisker trimming (D/DW) in Environment 2 (E2). Affected cells changed in rate-map correlation, grid score and/or peak-rate-position shift. **g** Spatial information of spatial cells decreased after trimming (same test; n = 613 spatial cells). **h** Affected and resistant spatial-cell proportions for D/DW. Affected cells changed in rate-map correlation, spatial information and/or peak-rate-position shift. Resistant cells in (**f**, **h**) changed in none of these metrics. In (**a**–**e**, **g**, **i**), center lines indicate medians, boxes the 25th–75th percentiles, and Tukey whiskers the most extreme values within 1.5 × IQR; beyond-whisker values are plotted individually. **i** Mean absolute error (MAE) of position decoding using a decoder trained on population activity of all spatially modulated cells in session D (RM one-way ANOVA with Geisser–Greenhouse correction and two-sided Tukey tests; n = 12 FOVs from 10 mice). **j** Representative actual (red) and decoded (blue) x-positions in D and DW; MAE is indicated. **k** Representative trajectories, rate maps and autocorrelograms of grid cells across D and DW. G and P indicate grid score and peak event rate; FOV crops across sessions are shown on the right. Scale bar, 10 µm. **l** Representative trajectories and rate maps for spatial cells; I and P indicate spatial information and peak rate. **m** Proportions of resistant HD, border, grid and spatial cells in E1 and E2, with resistant and total counts indicated (two-sided Chi-square test). $^{****}P \le 0.0001$; $^{***}P \le 0.001$; $^{**}P \le 0.01$; $^{*}P \le 0.05$; ns, $P > 0.05$. See Supplementary Data 1 for exact P values and detailed statistics. Source data are provided as a Source Data file.

significantly greater reduction in spatial information compared to non-ROI spatial cells following whisker trimming (Fig. 6j). Moreover, spatial fields located within the ROI were more likely to disappear than those outside the ROI (Fig. 6k–l). Together, these results suggest that tactile floor cues contribute to stabilizing spatial representations, and that removal of whisker-mediated tactile input preferentially disrupts the coding of fields anchored to the salient landmarks.

Cross-day stability modestly predicts vulnerability to sensory deprivation

We next asked whether the cross-day stability of spatially modulated cells in the tactile cue–dominated environment could predict their sensitivity to subsequent whisker trimming. The three mice used for five-day longitudinal imaging in Environment 2 also underwent whisker trimming on the final recording day. For each cell, we related the whisker trimming–induced change in tuning strength or map stability to its baseline variability across the five pre-trimming recording sessions.

For HD cells, whisker-trimming-induced reductions in tuning strength (ΔMVL, D/DW) were significantly correlated with cross-day variability (SEM of MVL across five days), such that cells exhibiting greater baseline variability showed larger deprivation-induced declines (Supplementary Fig. 12a, left). Moreover, cells with higher cross-day stability (mean correlation across five days) exhibited better preservation of tuning after trimming (Supplementary Fig. 12a, right). In contrast, no significant relationships were observed for border cells (Supplementary Fig. 12b). For grid cells, deprivation-induced reductions in grid score were significantly associated with cross-day variability, although the cross-day spatial correlation did not predict the magnitude of trimming effects (Supplementary Fig. 12c). Finally, spatial cells showed no significant association between cross-day stability and deprivation-induced changes in spatial information or spatial

https://doi.org/10.1038/s41467-026-78000-2

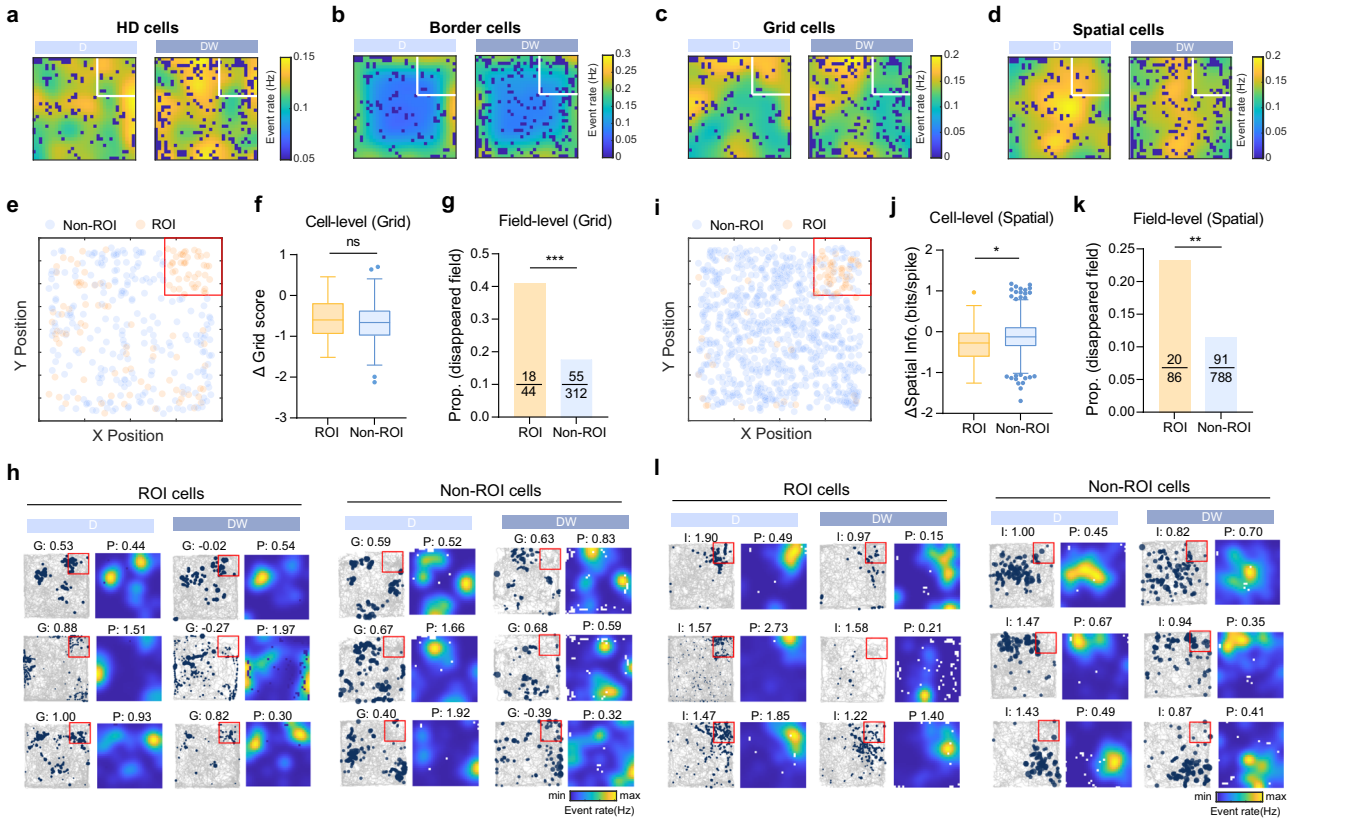


Fig. 6 | Fields anchored to dominant tactile floor cues are preferentially disrupted by whisker trimming. a–d Population-averaged rate maps for HD, border, grid and spatial cells in darkness (D) and darkness after whisker trimming (DW) in environment 2. Event rates were averaged across cells within each spatial bin. White squares indicate the tactile floor-cue region. **e** Distribution of grid fields, with field centroids located within the floor tactile cue region classified as region-of-interest (ROI) fields (orange) and all others classified as non-ROI fields (blue). The tactile cue region is outlined by the red box. **f** Cell-level comparison of changes in grid score ((Δ = DW − D)) between ROI grid cells and non-ROI grid cells. Grid cells with at least one field in the tactile cue region were classified as ROI cells (two-sided Welch's *t*-test; $n = 44$ ROI and 120 non-ROI cells). **g** Comparison of the proportions of disappeared ROI and non-ROI grid fields after whisker trimming (40.91% vs. 17.63%, Chi-square test). Field disappearance was defined as described in the Methods. **h** Trajectories and rate maps of representative ROI and non-ROI grid cells across D and DW. Red boxes mark the floor tactile cue region. G and P denote grid score and peak event rate. **i** Distribution of spatial-cell field centroids, displayed as in (**e**). **j** Spsuiteatial-information changes for ROI and non-ROI spatial cells (two-sided Welch's *t*-test; $n = 52$ ROI and 561 non-ROI cells). Spatial cells with their largest field in the tactile cue region were classified as ROI cells. In (**f**, **j**), center lines indicate medians, boxes the 25th–75th percentiles, and Tukey whiskers the most extreme values within 1.5 × the interquartile range; beyond-whisker values are plotted individually. **k** Comparison of the proportions of disappeared ROI and non-ROI spatial fields (23.26% vs. 11.55%, Chi-square test). **l** Representative ROI and non-ROI spatial cells, displayed as in (**h**). I and P denote spatial information and peak event rate. $^{****}P \le 0.0001$; $^{***}P \le 0.001$; $^{**}P \le 0.01$; $^{*}P \le 0.05$; ns, $P > 0.05$. See Supplementary Data 1 for exact *P* values and detailed statistics. Source data are provided as a Source Data file.

correlation (Supplementary Fig. 12 d). Together, these results indicate that long-term representational stability modestly predicts vulnerability to sensory deprivation in a subset of tuning metrics, particularly for HD and grid cells. Thus, while tactile cues can support stable spatial representations in darkness, cells with less stable baseline tuning are more susceptible to disruption following whisker-mediated sensory loss.

Environmental boundaries provide dominant stabilizing input after multisensory deprivation

Although visual cues were absent in Environment 2, a subset of cells were still able to maintain stable firing patterns following whisker trimming, showing no detectable changes in any tuning metrics (Fig. 5f, h and Supplementary Fig. 11g, j). Given the complexity of the rodent somatosensory system, tactile inputs beyond whiskers—such as those conveyed via the paws or nose—may contribute to sustaining residual spatial representations. We therefore examined whether plantar tactile input supports spatial coding under whisker deprivation. Because complete elimination of paw sensation is technically impractical and would likely disrupt locomotion, we instead removed the dominant floor tactile cue—the sandpaper patch—which constituted the most salient remaining plantar-accessible landmark after whisker trimming. Four mice re-explored the arena under this condition (DWR; Supplementary Fig. 13a). Removal of the sandpaper patch did not induce additional significant changes in tuning metrics across spatially modulated cell types (Supplementary Fig. 13b–h), nor did it impair positional decoding accuracy (Supplementary Fig. 13i). Importantly, this manipulation reduced—but did not abolish—plantar tactile input.

Environmental boundaries are known to provide strong corrective signals for path integration[11]. In the arena lacking other salient protrusions, the remaining tactile feedback may be predominantly derived from physical contact between the animal's nose or body and the surrounding walls. To assess the contribution of boundary-derived input, we eliminated access to the walls while preserving the floor landmark. In six mice tested on an elevated platform, the arena walls were removed following the DW session (DWR'; Fig. 7a), preventing wall contact without altering the sandpaper cue. Under these conditions, spatial tuning was profoundly disrupted across all classes of spatially modulated cells (Fig. 7b–e and Supplementary Fig. 14a, b). The spatial information of grid cells, which had remained stable under darkness and whisker trimming, was significantly reduced following

https://doi.org/10.1038/s41467-026-78000-2

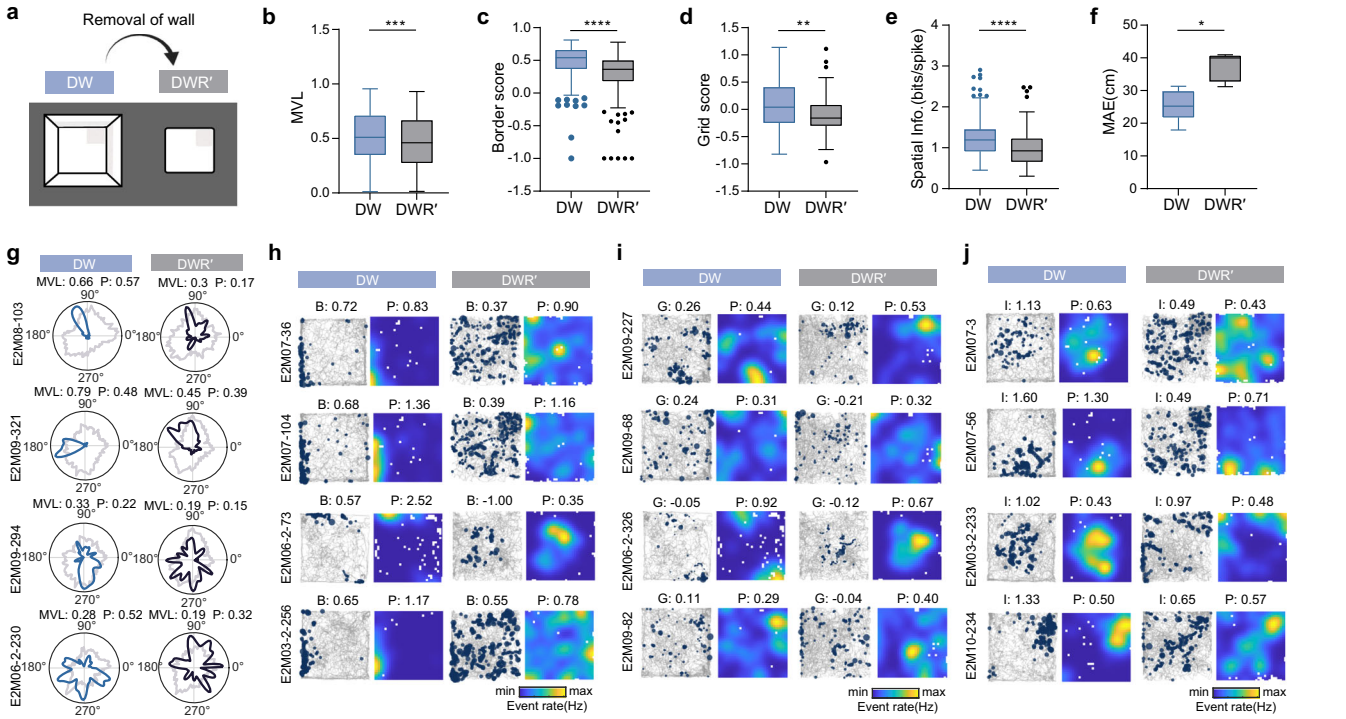


Fig. 7 | Removal of the arena wall significantly disrupts spatial representations following combined sensory deprivation. a Schematic of wall removal, showing the transition from darkness after whisker trimming (DW) to the wall-removed condition (DWR′). **b**–**e** Box plots comparing mean vector length (MVL) of HD cells, border score of border cells, grid score of grid cells and spatial information of spatial cells between DW and DWR′. Wall removal reduced all four tuning measures (two-sided Wilcoxon signed-rank tests; (**b**) $n = 276$ HD cells, (**c**) $n = 190$ border cells, (**d**) $n = 93$ grid cells and (**e**) $n = 327$ spatial cells). **f** Mean absolute error (MAE) of position decoding using a decoder trained on population activity of all spatially modulated cells from the baseline dark session. MAE increased after wall removal, indicating reduced decoding accuracy (two-sided Wilcoxon signed-rank test; $n = 6$ mice). In (**b**–**f**), center lines indicate medians, boxes the 25th–75th percentiles, and Tukey whiskers the most extreme values within 1.5 × the interquartile range; values beyond the whiskers are plotted individually. **g** Representative HD tuning curves from DW and DWR′. MVL and peak event rate (P) are indicated; corresponding cell-centered FOV crops are shown on the right. Scale bar, 10 µm. **h**–**j** Representative border, grid and spatial cells recorded in DW and DWR′. For each cell, trajectories are shown in gray and detected calcium events in dark blue; rate-map color indicates event rate. Border score (B), grid score (G), spatial information (I) and peak event rate (P) are indicated. ****$P \le 0.0001$; ***$P \le 0.001$; **$P \le 0.01$; *$P \le 0.05$; ns, $P > 0.05$. See Supplementary Data 1 for exact P values and detailed statistics. Source data are provided as a Source Data file.

wall removal (Supplementary Fig. 14c). Positional decoding errors increased markedly relative to the DW session (Fig. 7f and Supplementary Fig. 14d). Cells previously unaffected by whisker trimming (e.g., the first two HD cells in Fig. 7g) now showed significant changes in MVL and PFD, suggesting that their residual stability in DW sessions was supported by boundary-derived sensory feedback (Fig. 7g–j). Reapplying the wall-facing event-rate ratio analysis showed that border-cell wall-facing preference was no longer detectable in the DWR′ session (Supplementary Fig. 14e), suggesting that boundary-derived tactile feedback is important for maintaining border-cell firing under these conditions. Rather than remapping, most border cells, grid cells, and spatial cells failed to meet classification criteria following wall removal. Quantitatively, 50.7% (140/276) of baseline HD cells remained classifiable in session DWR′, whereas only 12.1% of border cells (23/190), 11.7% of grid cells (11/94), and 15.5% of spatial cells (51/328) met classification thresholds, highlighting the strong dependence of allocentric spatial coding on boundary information.

In two of six mice, exploration trajectories became biased toward the sandpaper region after wall removal, which closely matched the size and shape of the tactile patch (Supplementary Fig. 14f). Although observed in a subset of animals, this pattern suggests that, in the absence of boundary cues, the floor landmark may serve as a residual spatial reference detectable via plantar sensation. Population-averaged border-cell maps showed reduced firing along former arena boundaries but increased activity along the edges of the sandpaper patch in DWR′ (Supplementary Fig. 14g, top). After normalization, a new firing band emerged along the vertical edge of the tactile cue (Supplementary Fig. 14g, bottom), indicating a highly complex and adaptable spatial representation system in the MEC. In this context, animals may rely on plantar tactile input to detect the remaining sandpaper landmark on the floor and strengthen the encoding of that boundary.

A subset of MEC neurons shows activity covarying with whisker movement

During free exploration, rodents use their whiskers bilaterally to interact with objects, providing essential tactile inputs. Previous research has shown that the CA1 region of the hippocampus responds to both mechanical and passive whisker stimulation, potentially contributing to the updating of the spatial cognitive map[27]. Furthermore, it has been established that place fields in the hippocampus are modulated by tactile inputs from whiskers, although there is variability among individual cells[5]. We therefore performed an exploratory analysis to examine whether MEC neuronal activity covaries with whisker movement, which may reflect signals related to tactile sensing.

We conducted whisker-related experiments in ten male mice, three of which had also undergone whisker trimming in Environment 2. Each animal participated in three experimental sessions (Supplementary Fig. 15a). In the “spontaneous-whisking” session (Spont.), mice were head-fixed, and their spontaneous whisker movements along with corresponding neuronal activity were recorded simultaneously. Due to limited whisker movement under head-fixed conditions, we

performed an additional "stimulated-whisking" session (Stim.), during which an automated telescopic rod with a sandpaper sheet at its end was used to enhance whisker activity at regular intervals. In the final "free exploration" session, mice were allowed to explore an open field, enabling us to assess the spatial coding properties of the neurons recorded in the previous sessions. Given that whiskers on the same side exhibit highly similar movement[42], we selected the most distinguishable whisker for each animal for further analysis. To minimize false positives resulting from the low whisker movement observed during the "spontaneous-whisking" session, we primarily used data from the "stimulated-whisking" session to identify whisker-responsive cells, with the "spontaneous-whisking" session serving to validate our findings. The position of the selected whisker was extracted from each frame, and the corresponding angular position (θ) was calculated. Angular velocity (θ') was derived by calculating the change in angular position between two adjacent frames. We referred smoothed angular velocity (θ') as whisker movement and further calculated its Pearson correlation coefficient with each neuron's denoised ΔF/F trace (see Methods). We used this correlation-based approach because the limited temporal resolution of calcium imaging does not allow reliable assessment of neuronal activity changes over short intervals after tactile stimulation. To identify whisker-responsive cells, both correlation strength and within-session stability criteria were applied (see Methods). Specifically, the correlation between θ' and neural activity was calculated separately for the first and second halves of the "stimulated-whisking" session. Only neurons whose correlation coefficients exceeded the 95th percentile of the shuffled distribution in both halves were classified as whisker-responsive (Resp.) cells; all others were categorized as whisker-non-responsive (Non-Resp.) cells.

Of the 2187 recorded neurons, 191 (8.7%) were identified as whisker-responsive cells, whose calcium activity was positively correlated with whisker movement (Supplementary Fig. 15b, c). In an independent spontaneous-whisking session, these whisker-responsive cells also exhibited significantly higher correlations with whisker movement compared to whisker-non-responsive cells (Supplementary Fig. 15d), although correlation values were reduced relative to the stimulated-whisking session, likely due to weaker whisker activity in the absence of stimulation (Supplementary Fig. 15e). When correlations were recalculated using deconvolved calcium signals instead of denoised ΔF/F traces, whisker-responsive cells still showed significantly higher correlations than non-responsive neurons (Supplementary Fig. 15f), and this effect was consistently observed across both independent sessions (Supplementary Fig. 15g, h). These whisker-responsive cells showed calcium activity that covaried with whisker movement in both head-fixed sessions (Supplementary Fig. 15i). In addition, whisker-responsive cells exhibited a modest tendency toward anatomical clustering (Supplementary Fig. 15j, k; see Methods), which may reflect potential local connectivity.

Among the identified whisker-responsive cells, the majority (67.0%) did not exhibit spatial tuning during free exploration. The remaining 63 of 191 cells (33.0%) displayed spatially modulated properties, with HD cells comprising the largest fraction (17.3%), followed by border cells (12.0%), spatial cells (2.1%), and grid cells (1.6%) (Supplementary Fig. 16a). Because the total number of each spatially modulated cell type differed, we assessed whether the observed overlap between whisker-responsive cells and spatially tuned populations deviated from chance expectation. Using the overall proportion of whisker-responsive cells and the total counts of each cell type, we calculated the expected overlap under a hypergeometric distribution and compared it with the observed values. This analysis revealed significant enrichment of border cells, along with significant depletion of grid cells and spatial cells (Supplementary Fig. 16b). Representative examples showed that some whisker-responsive cells lacked detectable spatial tuning during free exploration (Supplementary Fig. 16c), whereas others were classified as HD, border, grid, or spatial cells based on their activity during free exploration (Supplementary Fig. 16d).

Additionally, we replicated the stimulated-whisking session in four independent mice under head-fixed conditions using a high-speed infrared camera (120 Hz) to more precisely capture whisker movement. A population of neurons exhibiting strong correlations between neuronal activity and whisker angular velocity was again identified, consistent with our initial findings (Supplementary Fig. 17a). The correlation strength of whisker-responsive cells did not differ significantly between the two experimental setups (Supplementary Fig. 17b). In this experiment, we also employed a secondary infrared camera positioned laterally to record paw movements and compute paw velocity, which served as an indicator of the animal's body locomotion. Although some whisker-responsive cells displayed calcium activity patterns closely resembling whisker angular velocity, their correlations with paw movement were minimal or absent (Supplementary Fig. 17c). These examples suggest that the activity of at least a subset of whisker-responsive cells was more closely associated with whisker movement than with broader body-movement-related signals. However, because whisker movement can covary with orofacial movements, arousal, and other behavioral states, these data do not exclude the possibility that some whisker-responsive activity reflects non-whisker-specific behavioral variables. Further experiments will be required to determine whether these signals specifically reflect tactile input or active tactile sensing.

Discussion

Effective spatial navigation is fundamentally dependent on reliable references, which are derived from both internal and external sensory information[43]. When spatial representations were established in a visual cue–dominated environment, light deprivation altered the representations of all spatially modulated cell types, whereas subsequent whisker trimming in darkness had more limited additional effects, particularly on grid and non-grid spatial cells. In contrast, in a dark tactile cue–dominated environment, all cell types could anchor their firing to tactile landmarks and form stable representations; under these conditions, grid-cell and spatial-cell representations became more sensitive to whisker trimming. In addition to whisker-mediated input, tactile signals conveyed through the nose or plantar surface may also contribute to maintaining spatial representations, particularly when visual and whisker-mediated cues are unavailable. Consistent with this idea, removing the arena walls to eliminate boundary-related tactile feedback markedly disrupted representations across all spatially modulated cell types. Together, these findings underscore the complexity of sensory integration in spatial navigation and highlight flexible strategies employed by the MEC to process external sensory information under varying environmental contexts. Finally, we identified a subset of MEC neurons whose activity covaried with whisker movement, suggesting that whisker-related signals may be represented in MEC. Further experiments are needed to determine whether these signals reflect tactile input and how they contribute to tactile cue-supported spatial navigation.

All known types of spatially modulated cells are modulated to varying degrees by sensory information, with HD cells being particularly sensitive. For instance, HD cells in the subiculum respond to environmental rotation[44]. In blind mice, HD cells in the anterior dorsal nucleus (ADN) use olfactory cues to finely encode head direction[36]. Moreover, disruption of vestibular input impaired the head direction tuning in the anterior thalamus[45], leading to subsequent effects on the place cells in the hippocampus[46]. Our results showed that head-direction tuning in the MEC was impaired following the deprivation of visual and whisker-mediated tactile inputs (Fig. 1 and Supplementary Fig. 3). The disruption observed under light deprivation may be explained by both direct and indirect anatomical connectivity between the MEC and visual cortical areas[47,48], which provide a pathway through

which visual information can influence spatial representations. In addition, it is well established that visual landmarks exert strong control over head direction tuning[49,50]. Numerous studies have demonstrated that removal of visual cues degrades HD stability[22], whereas reintroduction of visual landmarks restores directional tuning[23,51]. However, we did not observe a robust recovery of HD tuning following light reinstatement after whisker trimming. This persistent impairment likely reflects the sustained consequences of whisker deprivation on the HD network, such that only a subset of cells whose directional tuning was primarily governed by visual input—and thus minimally affected by whisker trimming—were able to recover their tuning strength following light reinstatement (Supplementary Fig. 3i). Moreover, in some animals, LDA revealed that, although the HD population activity did not return to its initial state following light reinstatement, it nevertheless retained the capacity to encode head direction within LW session (Supplementary Fig. 3j). This may suggest that, after an extended period of altered sensory experience between the two light sessions, HD population activity tends to stabilize around a shifted attractor state once visual input is reintroduced[49,52]. Whiskers are important for environmental exploration, allowing rodents to sample surface textures, contours, obstacles, and nearby boundaries. These tactile cues may contribute to spatial representations and support HD tuning within a cognitive map. In addition, whisker activity is closely linked to head movements in rodents, with the right-left asymmetry of whisker positioning preceding head movement[53], enabling obstacle detection and direction determination. Head turns and eye movements are flexibly coordinated, allowing animals to effectively integrate visual, vestibular, and somatosensory information[53–55]. In our study, whisker trimming resulted in a measurable reduction in head angular speed (Supplementary Fig. 4i), which may reflect compromised balance or altered vestibular input during head turns. This reduction may affect the activity of angular velocity cells[56,57]—potentially involved in vestibulo-ocular reflex and in maintaining or updating head direction tuning[38]. Therefore, the effect of whisker trimming on HD tuning, especially in Environment 1, may partly reflect changes in self-motion-related input in addition to reduced tactile information. Thus, HD cells likely integrate multimodal sensory inputs together with self-generated signals to maintain accurate directional coding.

Border cells, another crucial type of spatially modulated cell, are also impacted by light deprivation and whisker trimming (Fig. 2 and Supplementary Fig. 11). Animals may rely on visual cues to estimate their distance from environmental boundaries, and prior studies have shown that boundary-related firing fields can persist even when boundary information is provided predominantly through visual input[58]. However, direct contact with walls via whiskers may allow border cells to refine their firing fields with greater spatial precision. Because environmental boundaries provide corrective signals for path integration, and border cells are thought to contribute to this process by modulating grid-cell firing fields[11], our findings suggest that boundary-dependent spatial coding is sensitive to the quality of available sensory input. In darkness, the precision of distance estimation based on vision is reduced, and whisker trimming may further degrade boundary-related feedback. Consistent with this interpretation, we observed that border cells preferentially fired when the animal was oriented toward the wall (Supplementary Fig. 6f, g). Notably, this directional bias was completely abolished when the surrounding walls were removed (Supplementary Fig. 14e), and most border cells lost spatially specific firing rather than merely exhibiting remapping (Fig. 7h). This result differs from that reported by Solstad et al. [16], likely because in our wall-removal sessions, animals lacked both visual cues and the ability to detect environmental boundaries via whisker contact. Under these conditions, boundary-related sensory information was almost completely eliminated. These findings indicate that the maintenance of boundary fields depends strongly on external sensory inputs.

In the illuminated Environment 1 containing salient visual cue cards, spatial representations were likely established primarily on the basis of visual information. Under these conditions, removal of visual cues markedly altered firing patterns in grid cells and spatial cells, whereas further whisker trimming, after visual input had already been removed, produced only limited effects (Fig. 3 and Supplementary Fig. 8). In contrast, Environment 2 lacked visual input but contained a salient polarized tactile landmark. In this context, tactile cues likely contributed both to anchoring firing fields and to correcting accumulated path integration errors in the absence of vision. Accordingly, whisker trimming in Environment 2 had more pronounced effects on both grid and spatial cells, accompanied by alterations in field properties and decreased positional decoding accuracy (Fig. 5a–l). Moreover, when multiple tuning metrics were considered jointly, the proportion of HD cells, grid cells, and spatial cells that maintained stable tuning in Environment 2 was significantly lower than the proportion of whisker-trimming-resistant cells observed in Environment 1 (Fig. 5m). These findings suggest that the MEC flexibly constructs spatial maps depending on the dominant sensory modality available in the environment. Spatial representations primarily anchored to tactile information appear more vulnerable to whisker deprivation than those supported by vision.

Unlike vision, which originates from retinal photoreceptors, tactile inputs arise from mechanoreceptors distributed across the body rather than being confined to whisker follicles[59]. Consequently, whisker trimming alone cannot abolish all somatosensory input, consistent with the persistence of spatial selectivity in a subset of cells under combined darkness and whisker deprivation. Additional removal of surrounding walls further destabilized spatial coding (Fig. 7 and Supplementary Fig. 14), suggesting that somatosensory signals from the nose also contribute to navigation. Whereas boundary manipulations have been shown to induce grid-cell remapping[16], our results reveal a more severe outcome: when visual input, whisker-mediated tactile input, and boundary-related physical feedback were eliminated in the DWR′ condition, most grid cells lost their hexagonal firing patterns and most spatial cells lost their spatial selectivity. Nevertheless, a minority of spatially modulated cells remained classifiable, indicating that self-motion-related signals—such as vestibular and speed inputs—can partially sustain spatial representations when external sensory cues are drastically reduced. Notably, the disruption caused by single sensory deprivation was milder than that caused by medial septum inactivation or passive transport, both of which abolish grid-like firing entirely[60,61]. Thus, selective deprivation of individual modalities produces partial degradation of grid firing, whereas collective reduction of sensory inputs—particularly the elimination of boundary perception—profoundly disrupts spatial coding. Importantly, our manipulations likely did not eliminate all somatosensory input. Tactile signals from the paws were attenuated by removing the primary sandpaper landmark, and inputs from the nose were reduced by wall removal; however, residual somatosensory information may have persisted. Future studies employing more direct circuit-level interventions, such as transient inactivation of somatosensory pathways, will be required to more definitively establish the causal contribution of tactile signals to spatial representations.

Facial whiskers are vital sensory organs for nocturnal rodents like mice and rats, providing essential tactile inputs. The active movement of whiskers, known as whisking[62], facilitates environmental exploration and triggers sparse neuronal activity patterns in the primary somatosensory cortex (S1)[63]. Previous research has shown that rodents can use their whiskers to assess aperture widths with an accuracy finer than 5 mm[64]. Additionally, blind rats rely heavily on whisker input for gap crossing, and the same is true for sighted rats in darkness[30]. Moreover, whisker-mediated tactile input has also been implicated in

hippocampal function and spatial navigation. Whisker deflection-evoked responses observed in hippocampal CA1 imply that tactile inputs are transmitted to this area via the somatosensory cortex, contributing to experience-dependent learning[65]. Permanent whisker removal reduces hippocampal neurogenesis and impairs spatial memory[66]. The hippocampal CA1 region responds to whisker stimulation, likely contributing to the update of the spatial cognitive map[27]. Additionally, place fields are modulated by tactile inputs and can be disrupted by whisker pad inactivation[5]. Given the strong hippocampus–MEC connectivity, these findings raise the possibility that whisker-related signals may influence MEC spatial coding. Although direct monosynaptic projections from S1 to MEC have not yet been confirmed anatomically, several multisynaptic pathways may mediate this communication. For instance, the perirhinal and postrhinal cortices receive extensive somatosensory input and project heavily to MEC[67–69]. Additionally, thalamocortical circuits involving the posterior thalamic nucleus—known to process vibrissal information—may modulate MEC activity indirectly via these cortical areas[70]. Furthermore, the claustrum (Cla) provides the MEC with multisensory information, including information from the primary motor cortex (M1), primary visual cortex (V1), and S1, thereby potentially influencing its spatial coding process[71]. Consistent with a potential role of whisker-related signals in spatial coding, our exploratory analysis identified a subset of MEC neurons whose activity covaried with whisker movement (Supplementary Figs. 15–17), indirectly supporting the possibility that MEC could integrate tactile information into spatial navigation. However, because whisker movement can covary with broader orofacial movements, arousal, and other behavioral states, the present data cannot fully distinguish whisker-specific tactile signals from these related behavioral variables. Future studies using approaches with higher temporal resolution and more controlled tactile stimulation paradigms will be needed to more precisely characterize MEC responses to whisker-mediated tactile inputs.

Methods

Animal subjects

Our study used 37 adult male wild-type C57BL/6 N obtained from the Laboratory Animal Center of Peking University and Beijing Vital River Laboratory Animal Technology Co., Ltd. (Beijing, China). Sex differences were not evaluated because female mice were not included in the experimental design. Only male mice were used because prolonged 3–4-h open-field recordings required sustained locomotion and adequate arena coverage, which male mice more consistently achieved under our experimental conditions. This choice was also consistent with the predominantly male cohorts used in previous studies in the field. Thirteen mice were used for the L-D-DW-LW experiment in the visual cue–dominated environment (Environment 1, E1), and three additional mice were used for the L-D-DW control experiment in E1. Ten mice were used for the D-DW experiment in the tactile cue–dominated environment (Environment 2, E2). Among these ten mice, three underwent calcium imaging for five consecutive days, and two underwent a second round of whisker trimming after their whiskers had regrown following the initial trimming. Three mice from the E2 D-DW cohort, together with three additional mice, were also included in the tactile-cue rotation experiment. Of the 29 mice that underwent open-field experiments, six were also included in the whisker-related experiments. Eight additional mice were used exclusively for the whisker-related experiments. The Peking University Animal Use and Care Committee approved all procedures, which adhered to the guidelines set by the Association for Assessment and Accreditation of Laboratory Animal Care. The mice were individually housed under a 12 h light/dark cycle at a temperature of 22 °C and a humidity of 50%, with unrestricted access to food and water. A running wheel was placed in the cage to enhance the mice's activity. Behavioral experiments were conducted during the dark phase. Mice were 9–11 weeks old at the time of surgery and 12–32 weeks old during the experimental period.

Surgery

The surgical protocol was refined based on previous research[72]. Mice were initially anesthetized in a glass chamber with isoflurane, fixed in a stereotaxic frame, and continuously maintained under anesthesia through a mask delivering 1.2% isoflurane at 0.2 L/min. During the experiment, erythromycin ophthalmic ointment was applied to prevent corneal damage. An appropriate portion of scalp was resected to expose the skull's dorsal surface and the exposed skull surface was cleaned. A rectangle craniotomy measuring 2.0 mm in length and 1.4 mm in width was created over the right hemisphere, with its proximal edge centered 2.7 mm lateral to the midline and its distal edge located 4.0 mm lateral to the midline. The muscle near the craniotomy was carefully detached from the skull by surgery scissors. 600 nL of either rAAV-hSyn-GCaMP6f-WPRE-hGh polyA or rAAV-hSyn-GCaMP6s-WPRE-hGh polyA was injected at a rate of 100 nL/min using a glass capillary (NANOLITER2020 Injector, World Precision Instruments, FL, USA), with the injection site located 3.1 mm lateral to the midline, 0.3 mm anterior to the superior margin of the transverse sinus, and 1.7 mm below the brain surface. The capillary was left in place for 10 min to let virus spread. Similarly, another 600 nL virus was injected 3.7 mm lateral to the midline, 0.3 mm anterior to the transverse sinus, and at a depth of 1.5 mm below the brain surface.

The interface of the brain and the cerebellum was found and a pocket between the brain and the cerebellum was created by a surgical forceps while the cortical dura remained intact. A prism with its custom-made holder was connected to a stereotactic micromanipulator (1760, Kopf, CA, USA) and tilted 10 degrees laterally to ensure the imaging surface of the prism was parallel to the brain's dorsal surface. The prism assembly, consisting of a customized 1 mm diameter GRIN (gradient-index) lens attached to a 1 mm square prism (Grintech, Germany), was slowly inserted to the previously made pocket (subdural space within the transverse fissure). During implantation, the prism assembly was slowly lowered and moved in the anterior direction until the imaging plane of the prism was flush against the brain. Kwik-cast (World Precision Instruments, FL, USA) was used to seal the junction of the prism and exposed brain tissue. The scalp and the skull were adhered together using tissue adhesive (3 M, MN, USA). Then, dental cement was used to cover the full skull and a head bar was firmly fixed.

Experiment

Training process. After recovering from surgery, the mice were kept under a food-restriction regime, maintained at 80–90% of their normal body weight and given adequate water. For Environment 1, the arena was an 80 × 80 cm^2 white floor box, with three visual cue cards pasted on the three walls of the box. A camera was placed above the open-field to track animal's movement and two LEDs were used to emit either a white light or infrared light. Before the formal experiment, mice were trained to get familiar with the experimental environment for about one week. During the first adaptation stage, the mice freely ran in the open-field with no burden on the head. The experimenter stood outside and randomly sprinkled cookie crumbs into the arena to attract mice to forage for food. After mice were accustomed to persistently running in the box and had a good trajectory coverage, the training moved to the next stage. During this stage, the mice ran in the box with the optical fiber connected to its baseplate on the head and a helium balloon was attached to the fiber in an appropriate place to balance the weight. After they got used to running with the fiber and gained good performance, the formal experiment began.

For mice in Environment 2, all training and calcium imaging recordings were performed under dark conditions to minimize visual cues. The white open field arena was similar in shape and size to that

used in Environment 1 but contained no visual cue cards. To provide tactile cues, two vertical strips of white sandpaper with different grit sizes (approximately 15 cm in height) were attached to two walls of the arena, and a square piece of white sandpaper (~25 × 25 cm^2) was placed in one corner. The arena was positioned inside a behavioral chamber and enclosed with black curtains.

Open-field experiments. Calcium imaging was performed with the miniature two-photon microscope[35] (LFMTPM-V2.0.1; working distance: ~1 mm, NA: 0.45). Before imaging, the cover of the GRIN lens on the prism was removed, the gel was added to cover the surface of lens and then microscope was placed into the baseplate and locked with screws. Calcium indicators were excited at 920 nm, with the laser intensity ranging from 50 to 80 mW at the sample. Image acquisition was managed using GINKGO-MTPM (Transcend Vivoscope Biotech Co., Ltd, China). Images (600 × 512 pixels) were captured at a resolution of ~0.89 μm/pixel and a frame rate of 9–9.5 Hz with a femtosecond fiber laser (TVS-FL-01, Transcend Vivoscope Biotech Co., Ltd, China). Running trajectory was recorded through the camera on the ceiling at 25 Hz. Behavioral videos and calcium imaging videos were simultaneously acquired by software GINKGO-MTPM (Transcend Vivoscope Biotech Co., Ltd, China).

Experiments in environment 1 (E1). The Light–Dark–Dark, Whisker-trimmed–Light, Whisker-trimmed (L-D-DW-LW) experiment was conducted continuously within one day. In the first session (L), neuronal activity was recorded as the mouse freely explored the open field with the warm-light LED on, to establish baseline spatial representations. In the second session (D), the light was turned off to create a dark environment, testing the influence of visual input. After completing the dark session, the mouse was head-fixed, and the experimenter quickly removed all its whiskers using scissors. The whisker-trimmed mouse was then placed back into its home cage to acclimate for a short period before the subsequent experiments began. Once the mouse resumed normal activities (e.g., running on the wheel), it was then reintroduced into the open field for the third session (DW) exploration, where the light remained off, and whisker-mediated tactile input was deprived. In the fourth session (LW), the light was turned on again to test whether the regained visual input could restore spatial cognition while tactile input was deprived. Ambient light intensity in the experimental environment was measured using a multi-source illuminance meter (DL333205; Deli Instruments, Ningbo, China; measurement range: 0–200,000 lux). During light conditions, illumination was maintained at 4.5–4.6 lux, whereas under dark conditions, light intensity was measured as 0.0 lux. The lengths of the longest macrovibrissae in the experimental mice ranged from approximately 2.6 to 3.1 cm prior to trimming. Each session lasted 25 to 40 min to ensure that the trajectory evenly covered the whole open field. Prior to formal recording, mice were placed in the open field for habituation and then removed. The walls and floor of the arena were thoroughly cleaned before the start of the experiment. For the three animals in which the microscope was detached between sessions D and DW, gel was applied to the lens surface before reinsertion.

Experiments in environment 2 (E2). For the rotation experiment, six male mice were first allowed to establish a stable representation of the tactile cue–dominated open field under dark conditions. The mice were then returned to their home cages. The arena was thoroughly cleaned by removing all feces and food debris with a vacuum cleaner, followed by careful wiping of the sandpaper, the floor and walls with alcohol. In addition, alcohol was sprayed into the air to minimize potential residual olfactory cues. Subsequently, the entire arena—including the primary tactile cues (sandpaper) as well as any subtle visual features on the floor and walls—was rotated 90° clockwise. The mice were then reintroduced into the rotated environment for a second recording session.

To directly assess the impact of whisker trimming in the tactile cue–dominated environment, we conducted an additional Dark-Dark, Whisker-trimmed task using 10 mice. In this task, animals were first allowed to establish stable spatial maps during a baseline dark session (D), followed by direct whisker trimming (DW). Two of the mice underwent a second whisker-trimming experiment after their whiskers had regrown to sufficient length, with imaging performed in a newly selected field of view. In addition, four mice in this cohort were tested in a DWR session following the DW session, in which the sandpaper attached to the floor was removed. The remaining six mice underwent a DWR′ session after the DW session, in which the arena walls (together with the attached sandpaper) were removed while the sandpaper on the floor was retained. All sessions for these six mice were conducted on a platform elevated approximately 20 cm above the ground.

Whisker-related experiment. For "stimulated-whisking" sessions, mice were fixed in a platform, whisker movements were recorded using a camera directly above the mice' heads at about 45 Hz and neuronal activity was simultaneously recorded by two-photon calcium imaging. A custom-built automatic stimulator was placed on the side of the mouse's cheek to enhance whisker movement, which contained an automatic telescopic rod with a piece of sandpaper at the end. Each "stimulated-whisking" session contained 10 continuous trials, each trial lasted for 1 min, consisting of 5 s of stimulation and 55 s of non-stimulation. During the stimulation period, the rod was extended so that the sandpaper sheet at the end could contact most of the mice's whiskers and the mice showed an increased frequency of whisker movement (see Supplementary Video 2). During the remaining non-stimulation period, the rod was in its retracted state and the whiskers had no contact with the sandpaper (see Supplementary Video 1).

For the spontaneous-whisking session, the setup was identical to that of the stimulated-whisking session, except that no stimulus was presented to the mice, that is, the rod was in its retracted state and the sandpaper was inaccessible to the whiskers. Mice showed less whisker movement in this session.

In a separate experiment (Supplementary Fig. 17), whisker movements were recorded from above using a high-speed camera (120 Hz), while a lateral camera simultaneously recorded paw movements (Supplementary Video 3); all other aspects of the setup remained unchanged.

Histology. After completing all experiments, animals were anesthetized with isoflurane and perfused with saline followed by 4% paraformaldehyde (PFA). Skin and muscles were removed from the skull using surgical scissors. The skull was fixed in PFA for at least 24 h to preserve the brain, cerebellum, and prism implantation site without deformation. The brain was cryoprotected in 30% sucrose solution for 24 h before sectioning, and the remaining skull and prism were carefully removed. Sagittal sections (30 μm thick) were obtained using a cryostat (Leica).

Brain sections were stained with DAPI, and GFP immunostaining was performed in selected mice. For GFP immunostaining, sections were first blocked in PBS containing 10% goat serum and 0.3% Triton X-100 for 1 h. Sections were then incubated overnight at 4 °C with chicken anti-GFP antibody (Thermo Fisher Scientific, catalog # A-10262, RRID AB_2534023; diluted 1:1000 in blocking solution). Subsequently, sections were washed three times with PBS for 5 min each and incubated with goat anti-chicken IgY (H + L) Alexa Fluor 488 secondary antibody (Thermo Fisher Scientific, catalog # A-11039, RRID AB_2534096; diluted 1:1000 in blocking solution) for 2 h at room temperature. Finally, sections were washed twice with PBS for 5 min each and mounted with DAPI (Sigma-Aldrich, catalog # D9542). Stained sections and prism implantation sites were visualized using an

Olympus VS120 virtual slide microscope or Zeiss Axio Scan Z1. Images were further processed using OlyVia software (version 4.1.1; Olympus Corporation, Tokyo, Japan) and ImageJ (version 1.54p; National Institutes of Health, Bethesda, MD, USA).

Data analysis

Position tracking. DeepLabCut (version 2.3.10)[73,74] was utilized for tracking animals' position in the open-field. Six key points were labeled for each mouse: the nose tip, head center, left ear, right ear, mid-body, and tail base. The head direction was calculated based on the coordinates of the nose tip and head center. For each mouse, approximately 0.5% of behavioral videos from all recorded sessions were extracted to create the training dataset, resulting in around 600–1200 frames per model. A ResNet-50-based neural network[75] was employed with default parameters for 650,000 to 1,030,000 training iterations. All models achieved a test error of less than 4 pixels and a training error of less than 3 pixels (image resolution: 1008 × 964 pixels). Subsequently, a p-cutoff value of 0.6 was applied to filter low-confidence coordinate predictions. This trained network was then used to analyze videos from all the sessions in the open field experiments. After obtaining the analysis results from DeepLabCut, the predicted pose and skeletal structure were overlaid onto the corresponding frame, generating a new video file for researchers to visually inspect the model's performance. Additionally, in the subsequent analysis, frames in which the mouse's position was outside the open field arena or where the distance between the nose tip and head center exceeded 4 cm were excluded as outliers.

Calculation of behavior variables. Head angular velocity was calculated as the change in head direction angle between consecutive frames, divided by the elapsed time between frames (rad/s). Head angular acceleration was subsequently derived as the change in angular velocity between consecutive frames, similarly divided by the time difference (rad/s^2).

For all boundary-related analyses, the boundary region was specifically defined as the area extending 10 cm inwards from the walls of the square arena. This width was chosen as it is widely adopted in existing literature for investigating boundary-related neuronal activity[76–78].

To explore the relationship between border cell firing and the animal's perception of environmental boundary, we analyzed the firing patterns of border cells specifically during epochs when the animal was located within the border zone, and examined how the firing probability related to the animal's head direction. Calcium events were categorized as either $Event_{facing}$ (calcium events occurring when the animal's heading fell within a defined angular range directed toward the wall) or $Event_{away}$ (events occurring when the animal faced away from the wall) (Supplementary Fig. 6f). To account for potential behavioral biases in the animal's head direction distribution within the border zone, event counts were normalized by the corresponding dwell time in each heading category: $Heading_{facing}$ (total time spent facing toward the wall) and $Heading_{away}$ (total time spent facing away from the wall). The inward and outward event rates were thus defined as:

$$R_{\text{facing}} = \frac{Event_{facing}}{Heading_{facing}}, R_{\text{away}} = \frac{Event_{away}}{Heading_{away}} \quad (1)$$

A firing preference index C was then computed as the ratio of inward-to-outward event rate:

$$C = \frac{R_{facing}}{R_{away}} \quad (2)$$

A value of $C > 1$ indicates that the cell fires at a higher rate when the animal faces toward the wall than away from it. Only cells for which both $Heading_{facing} > 0$ and $Heading_{away} > 0$ were included in subsequent analyses.

"Wall approaching time" was calculated to quantify the proportion of total recording frames during which the animal engaged in direct wall contact behavior. This was specifically defined as instances where the animal's position was located within boundary area and its head was simultaneously oriented directly towards the wall (a head direction angle of ±45° relative to the wall normal).

Calcium signal processing. Image stacks from all sessions recorded within a single day were processed using Suite2p (version 0.14.4)[79], which performed motion correction, region of interest (ROI) detection, and calcium signal extraction. The raw fluorescence signal (F_{cell}) and the neuropil fluorescence signal (F_{np}) were directly obtained from the Suite2p output file (Fall.mat) and further analyzed using a custom MATLAB pipeline. F_{cell} and F_{np} represent the weighted averages of fluorescence within and surrounding an ROI, excluding pixels overlapping with other ROIs. The fluorescence time course of each cell was calculated by averaging pixel intensities within the ROI and correcting for neuropil contamination, with the corrected signal defined as[80,81]:

$$F_{raw} = F_{cell} - 0.7 \times F_{np} \quad (3)$$

Baseline fluorescence (F_0) was estimated using a moving-window method that smoothed the local 8th percentile fluorescence and applied a correction term for stability. This method is consistent with the approach described by Zong et al. (2022) [81]. The normalized fluorescence change ($\Delta F/F$) was then calculated as:

$$\Delta FF = \frac{F_{raw} - F_0}{F_0} \quad (4)$$

Artifacts were minimized by detecting and removing outliers based on z-scores. Wavelet-based denoising methods were applied to $\Delta F/F$ to further improve signal quality and obtain denoised $\Delta F/F$. Significant transients were identified as periods during which denoised $\Delta F/F$ exceeded twice the local standard deviation for at least 0.75 s, following the criteria established by Zong et al. Denoised $\Delta F/F$ signals were then deconvolved using the Online Active Set method to Infer Spikes (OASIS) algorithm[82,83], where the rise and decay time constants of calcium indicators were estimated automatically based on the fluorescence traces[83]. Frames containing significant transients were used to filter the raw deconvolved calcium activity (E_{raw}), yielding the filtered signal ($E_{filtered}$). The filtered calcium activity was normalized, and non-zero events were classified as "calcium events". The event rate was calculated as the number of calcium events per second for each cell. All subsequent spatial tuning analyses were performed using these deconvolved calcium events.

The signal-to-noise ratio (SNR) was determined as the ratio of the median amplitude of the 99th percentile of $\Delta F/F$ during significant transients to the standard deviation of $\Delta F/F$ during resting periods.

Calculation of tuning maps. For open-field experiments, the 80 × 80 cm^2 square was divided into 2.5 × 2.5 cm^2 bins to create spatial tuning maps, which represent neuronal activity normalized by occupancy. Each bin's value in the tuning map was calculated as the ratio of the total calcium events to the duration spent in that bin. A Gaussian filter was applied to smooth position data. Arena coverage was defined as the proportion of visited bins to the total number of bins, with a bin considered visited if the animal spent at least 0.1 s there. To eliminate the effects of behavioral state changes (e.g., foraging versus resting), data points with running speeds below 2.5 cm/s or above 60 cm/s were excluded from all analyses of both observed and shuffled data. Head-direction tuning maps were developed using similar methods (Range:

0–360°; bin size: 3°). These values were then smoothed using a Gaussian filter (standard deviation: 2.5 cm for spatial heatmaps and 2° for head direction tuning curve).

Spatial information content, measured in bits per event, was determined using the formula[84]:

$$\sum_i p_i \frac{\lambda_i}{\lambda} \log_2 \frac{\lambda_i}{\lambda} \quad (5)$$

where λ_i is the mean event rate in the i-th location bin, λ is the overall mean rate, and p_i is the probability of the animal being in the i-th bin. Head information is calculated using the same method, except that p_i in this case is the probability of the animal's head direction being in the i-th angle bin.

Grid cells. All grid cells were selected from the baseline session and assigned a grid score based on their autocorrelogram, as described by Sargolini et al.[14]. Briefly, each cell's autocorrelogram was rotated at multiple angles, and Pearson correlations were calculated for rotations at 60° and 120° (Group 1) and at 30°, 90°, and 150° (Group 2). The minimum difference between any element in Group 1 and any element in Group 2 was determined. The grid score for each cell was defined as the highest minimum difference between Group 1 and Group 2 rotations across all successive circular samples. The central peak was not included in the analysis.

Grid cells were identified using a shuffle-based approach. For each cell, the calcium event sequence was circularly time-shifted along the animal' s trajectory by a random interval to generate shuffled datasets, following methods described by Zong et al. [81] Additionally, for each cell, we recalculated the spatial tuning map for the first and second halves of the baseline session and computed the correlation between these two maps to assess intra-session stability. A cell was defined as a grid cell if its recorded grid score exceeded the 95th percentile of grid scores from the shuffled data and its intra-session stability was greater than 0.3 in the baseline session. Cells with a negative grid score were excluded from our data.

For detailed analysis of grid-cell geometric features, we examined grid spacing and calculated ellipticity for each grid cell under each experimental condition. Grid spacing was determined by measuring the distance from the center of each autocorrelogram to its six surrounding autocorrelation nodes, then averaging these distances. The standard deviation of grid spacing was calculated to reflect the regularity of grid pattern. To calculate ellipticity, an ellipse was fitted to the identified maxima using a least-squares method[85]. For cells where the fitting was successful, ellipticity was defined as the ratio of the semi-major axis to the semi-minor axis of the fitted ellipse, yielding a value between 1 (a perfect circle) and infinity (∞). Grid cells with ellipticity values > 5 were excluded from the ellipticity-related analysis.

Border cells. The border score was calculated to assess the spatial firing patterns of cells in relation to the environment's boundaries, based on previously described methods[16], with adjustments for calcium imaging data. Fields of a cell were identified using a threshold set at 30% of the maximum event rate within the map. The border score was then determined by calculating the difference between the highest coverage of any single field along any of the four walls and the average distance to the nearest wall for that field, weighted by event rate and normalized by half the shortest side of the environment. Border scores ranged from −1 to +1, with a score of +1 indicating cells with infinitely narrow fields perfectly aligned along the entire wall.

Border cells were identified based on their border scores significantly surpassing chance levels determined by a shuffling procedure, similar to that used for grid cells. A cell was classified as a border cell if its true border score exceeded the 95th percentile of scores from 1000 shuffled permutations of the same cell and the spatial correlation between the first and second halves of the baseline session was above 0.3.

Spatial cells. Spatial cells were characterized by a spatial correlation greater than 0.5 between the two halves of the baseline light session and spatial information content exceeding the 99th percentile of the shuffle distribution, excluding grid cells and border cells.

Head direction cells. All HD cells were selected from the baseline session. We calculated the mean resultant vector (mean vector length, MVL) from the head direction tuning curve following the method described by Sargolini et al[14]. A cell was considered to be modulated by head direction if its MVL exceeded a chance level established by repeatedly shuffling the experimental data for 1000 times. For each shuffle, the deconvolved calcium activity sequence was circularly time-shifted relative to the mice's head-direction sequence. We also assessed the intra-session tuning stability of HD cell candidates by calculating the Pearson correlation between the head direction tuning curves from the first and second halves of the session. A cell was identified as an HD cell if its MVL was larger than the 99th percentile of MVLs from its shuffled data and had an intra-session stability larger than 0.5. Head information was calculated as described above to measure the information about animals' head direction conveyed by an HD cell. If a cell met the criteria for both HD cells and grid cells, it was classified as a Grid × HD cell; otherwise, it was categorized as a pure HD cell.

Field extraction and ROI classification. Firing fields were identified from two-dimensional rate maps. A firing field was defined as a contiguous region comprising at least 30 spatial bins ($2.5 \times 2.5\ cm^2$ per bin) in which firing rates exceeded 20% of the cell's peak rate. Candidate regions were retained only if their peak rate was ≥ 0.1 Hz.

The tactile cue region (region of interest, ROI) was defined a priori as a $25 \times 25\ cm^2$ area located in the upper-right quadrant of the arena. Cells were classified according to the centroid location of their baseline firing fields. At the cell level, a grid cell was designated as an ROI cell if at least one field centroid fell within the ROI, whereas spatial cells were classified based on the centroid of the largest-area field. At the field level, each baseline field was independently categorized as ROI or non-ROI according to its centroid position. For each field in baseline dark session (D), the closest field in session DW within the same cell was identified, and spatial overlap was quantified as the proportion of baseline field pixels overlapping with the matched field. A field was considered disappeared if the overlap ratio was <0.2. In three animals, the tactile floor cue in the baseline session was rotated 90° clockwise relative to the other subjects. To standardize the tactile reference frame across animals, behavioral trajectories, event coordinates and spatial rate maps from these animals were rotated 90° counterclockwise prior to analysis.

Position decoding. Animal's position was decoded using a Naïve Bayes decoder[86] based on neural activity recorded in each session. We modeled events from different cells as independent Poisson and adopted a uniform prior for all spatial bins[87]. Calcium event data was reassigned into intervals of 1 s and smoothed using a 5 s time window. The average position of the animal across all frames within each time window was used to represent the mouse's position in that specific time bin. For each time bin, the probability of the animal being in a specific position bin was calculated using the formula:

$$P(X, |, \mathbf{n}) = CP(X)\left(\prod_{i=1}^{N} f_i(X)^{n_i}\right) e^{-\tau \sum_{i=1}^{N} f_i(X)} \quad (6)$$

where X is the spatial bin, the element n_i of vector $\mathbf{n} = (n_1, n_2, \ldots, n_N)$ is the number of calcium events for neuron i within each time bin, C is a

normalization factor, $P(X)$ indicates the overall probability of the animal occupying spatial bin X, $f_i(X)$ is the mean event rate of cell i in spatial bin X, and τ is the length of the time window. While the vector $\mathbf{n}$ was obtained from the test data, other variables were derived from training data. The position with the maximum likelihood was identified as the animal's decoded position for each time bin. The decoding error for test data was calculated as the mean absolute error (MAE) between the actual position and the decoded position.

For each mouse with n grid cells, we randomly selected k cells from 1 to the total number of grid cells n to establish a decoder for baseline session. This process was repeated 100 times to obtain the MAE of the decoder with k cells. We observed that the MAE gradually decreased as k increased, indicating an improvement in the decoder's performance (Supplementary Fig. 7f, top). Ultimately, we selected four mice with more than 20 grid cells each for subsequent statistical analysis related to decoding (Supplementary Fig. 7f, bottom).

The first half of the baseline light session served as the training set, while the second half was used as the test set to establish a basic spatial coding pattern before sensory deprivation. Subsequently, we decoded the animal's position using the second half of the following sessions (D, DW, LW) as the test set, based on the initial training set in baseline session, to investigate whether the spatial coding pattern of grid cells changed after sensory deprivation. A shuffled data set was created by randomly time-shifting the animal's position in the baseline light session 1000 times.

For the decoding analysis based on all functional cell types, the neuronal activity of HD cells, border cells, grid cells, and spatial cells was used, with the decoder construction method being the same as described above. The same procedure was used to construct the position decoder in Environment 2. The only difference was that the first half of the Dark baseline session was used for training, whereas the second half of the D, DW, DWR, and DWR′ sessions was used for testing.

Population vector (PV) correlation. To assess the change of population coding of HD cells after sensory deprivation, we computed the population vector correlation between session pairs. The head direction was first divided into 120 angle bins (3° each). For each bin, we calculated the corresponding population vector (PV) by concatenating the mean event rates of all HD cells associated with that bin. Subsequently, the Pearson correlation between PV for every possible pair of angular bins was calculated for each mouse, resulting in a correlation matrix for each session. Each value within this matrix represents the correlation between the PV of two specific angular bins. We then computed the mean correlation across all mice for each bin pair, yielding an averaged correlation matrix for each session pair. These averaged matrices were then combined into a single comprehensive matrix, which provides a visual representation of the consistency in head direction tuning across different sessions and angular bins (Fig. 1m). Additionally, we compiled the tuning curves of all HD cells into a 2-dimensional matrix for each mouse, referred to as the population vector matrix. The correlation between these PV matrices was computed across session pairs. The mean and SEM of the PV correlations for all mice ($n = 13$) are presented in Fig. 1n, with color representing the correlation values.

For border cells, we rearranged the 2D rate map of each cell into a 1D row vector and combined the event rates from all cells. This resulted in a 2D population vector matrix for each mouse in each session. We subsequently computed the PV matrix correlation between session pairs for each mouse. By averaging these data across all mice, we assessed the changes in the population coding of border cell after sensory deprivation (Fig. 2i).

Quantifying session-to-session changes at the single-cell level. To assess session-to-session changes in HD tuning at the single-cell level (baseline session i vs. condition session j, e.g., L to D), we used a resampling-based paired framework applied independently to each recorded cell. For each cell, we defined the analysis window length as half of the total duration of session i, and included cells only when session j lasted at least as long as this window duration. We then performed 100 iterations in which we randomly sampled a contiguous time window of this fixed length from session i and an independent time window of the same duration from session j, extracting calcium events and position samples within each window. To ensure data quality, sampled windows were accepted only if they contained at least 50 events; otherwise, we resampled up to 50 attempts per iteration, and iterations failing these criteria or yielding empty/invalid tuning estimates were treated as missing. For each accepted window, HD tuning curves were computed and tuning statistics were extracted to quantify multiple properties of HD coding. Specifically, changes in tuning strength were computed as changes in MVL, whereas directional drift across sessions was quantified as the absolute circular difference in PFD. In addition, tuning-curve similarity was assessed by comparing stability within session i (correlation between tuning curves computed from a randomly sampled window and its complementary time segment) against stability across sessions (correlation between the session i window and the matched-length window from session j). For all three metrics, statistical inference was performed independently within each cell using a paired one-tailed sign test across valid resampling iterations. For each cell, paired differences were computed between cross-session and within-session values, and the null hypothesis assumed that positive and negative differences were equally likely (Binomial distribution, $p = 0.5$). The direction of the one-tailed test was defined according to the specific hypothesis for each metric. Specifically, for tuning strength (MVL) and tuning-curve similarity (correlation), we tested whether session j exhibited a significant reduction relative to the within-session baseline of session i (i.e., cross-session values <within-session values). In contrast, for PFD drift, we tested whether cross-session directional deviation was significantly greater than the within-session deviation observed in session i. Resulting p-values were corrected across cells using the Benjamini-Hochberg false discovery rate (FDR) procedure. Cells were classified as showing a significant change at $q < 0.01$, additionally requiring that the median metric across iterations reflected the hypothesized direction of effect (i.e., median MVL or correlation decreased in session j, or median PFD deviation increased relative to within-session variability).

To quantify how many HD cells exhibited alterations in one or more aspects of tuning, each metric was binarized per cell (significant vs. not significant after FDR correction). Cells showing a significant change in any metric were then categorized into affected cells, and those showing no significant change in any metric were defined as resistant cells (Fig. 1l and Supplementary Fig. 11g).

A similar resampling-based framework and statistical logic were applied to grid cells, border cells, and spatial cells (Figs. 2h, 3h, 5f, 5h and Supplementary Fig. 11j). In these analyses, spatial rate maps were computed for each resampled window, and corresponding spatial metrics were extracted, including grid score, border score, and spatial information, depending on cell type. For grid cells, we tested whether the grid score in session j was significantly reduced relative to session i, whether the cross-session spatial rate map correlation was significantly lower than the within-session correlation of session i, and whether the absolute displacement of the peak firing location between sessions exceeded the displacement observed between two within-session resampled segments. For spatial cells, the same procedures were applied, with spatial information replacing grid score as the tuning-strength metric. For border cells, we examined whether the border score was significantly reduced, whether spatial rate map correlation decreased, and whether the distance between the peak firing location and the nearest environmental boundary increased in session j relative to session i.

LDA-based dimensional reduction. To investigate the structure of head-direction representation and its alteration under sensory deprivation, we applied linear discriminant analysis (LDA)[88], a supervised dimensionality reduction technique. LDA seeks an optimal linear transformation that maximizes between-class variance while minimizing within-class variance. In our study, we used an LDA-based method to project the high-dimensional neuronal activity on a 2-dimensional plane with best separation of head direction tuning.

First, we computed neural trajectories in an N-dimensional space using a binary matrix $\mathbf{A} \in \mathbb{R}^{N \times T}$ to represent the calcium events, where N is the number of identified head-direction cells in the baseline session, and T is the number of time frames. Each matrix element $[\mathbf{A}]_{i,j}$, indicates the present (1) or absence (0) of a calcium event for a neuron i at time j. We then divided the time frames into overlapping time bins, smoothing the data to reduce variance. Event rates of each neuron were calculated for each bin, and head-direction angles were assigned based on the direction nearest to the bin center, resulting in an N-dimensional neural trajectory matrix $\mathbf{B} \in \mathbb{R}^{N \times T'}$ and a corresponding head-direction array $\mathbf{H} \in \mathbb{R}^{T'}$. These were then subjected to LDA for dimensionality reduction.

LDA was trained using neuronal activity from the baseline light session to derive the optimal linear transformation. This transformation was then applied to neuronal activity from subsequent sensory-deprivation sessions to project all sessions into the same low-dimensional space, enabling direct comparison of head-direction representations across conditions (Fig. 1o and Supplementary Fig. 3f). The Fisher's linear discriminant ratio was used to quantify the separability of head-direction classes, and a separation index was used as an additional validation metric. To assess intra-session stability in the baseline light session, the transformation derived from the entire baseline session was applied separately to neuronal activity from the first and second halves of that session (Supplementary Fig. 3d).

Whisker-related analysis

Identification of whisker-responsive cells. Videos recording whisker movement were analyzed by Facemap (version 1.0.6)[89] or DeepLabCut[73] to extract the coordinates of the proximal and distal points of a selected whisker in each frame, hereafter referred to as the "root" and "tail" positions, respectively. The root and tail positions were determined by comparing the standard deviations of the initial position data, with the position set having a higher standard deviation designated as the tail, and the other as the root. The mean positions for both the root and tail points were calculated to establish the reference vector ($\mathbf{v}_0$) between these mean positions. For each frame, the vector ($\mathbf{v}_t$) between the root and tail positions was computed, and the angle between $\mathbf{v}_0$ and $\mathbf{v}_t$ was calculated as angular position (θ). Following the angle calculation, the angles were smoothed using a Gaussian filter with a window size of 2 s to obtain θ_{smooth}. Angular velocity (θ') was then calculated as the difference between consecutive smoothed angles divided by the corresponding time interval. The mean absolute values of θ' over each interval between consecutive calcium-imaging timestamps were then smoothed using a Gaussian filter with a window size of 1 s to obtain the final value of whisker movement. The whisker movement sequences of three distinct whiskers from the same animal were highly similar, supporting the consistency of the whisker-tracking method.

A cell was classified as whisker-responsive based on the Pearson correlation between its denoised $\Delta F/F$ trace and the whisker angular velocity sequence. To assess significance, a shuffle procedure was performed 1000 times. For each shuffle, the denoised $\Delta F/F$ trace was circularly shifted by a random temporal offset relative to the whisker movement, and the Pearson correlation was recalculated to generate a null distribution. To increase robustness, the stimulated-whisking session was divided into two equal halves, and the shuffle procedure was applied independently to each half. A cell was identified as whisker-responsive only if its true correlation exceeded the 95th percentile of the shuffled correlation distribution in both halves of the session.

Calcium imaging data collected from the free-exploration session, spontaneous-whisking session, and stimulated-whisking session were analyzed together using Suite2p to identify the same cells across these sessions and assign spatial coding identities based on activity recorded during the free-exploration session. The standards used for cell detection were consistent with those used in open-field experiments.

Anatomical analysis. To determine whether whisker-responsive cells exhibited anatomical clustering, we applied a nearest-neighbor (NN) distance-based permutation analysis, similar to approaches previously used to assess spatial organization of functionally defined cell populations[41]. Briefly, the anatomical location of each neuron was defined by the centroid of its spatial footprint extracted from Suite2p segmentation.

We restricted the analysis to animals with at least 10 whisker-responsive cells per imaging FOV to ensure reliable estimation of spatial statistics. For a given FOV, we computed the Euclidean distances between all pairs of responsive cells and quantified clustering using the mean distance to the k nearest neighbors ($k = 1–5$). For each neuron, the average distance to its k closest neighbors within the responsive population was calculated, and the global clustering statistic was defined as the mean of these per-cell nearest-neighbor distances. To evaluate whether the observed spatial organization deviated from chance, we performed a label-permutation test in which the anatomical positions of all recorded cells were held fixed while randomly assigning the whisker-responsive label to an equal number of cells drawn from the full population. For each value of k, 1000 permutations were generated to construct a null distribution of the mean k-NN distance expected under spatial randomness with preserved cell density. The empirical p-value was calculated as the proportion of shuffled datasets in which the mean k-NN distance was less than or equal to the observed value (left-tailed test). Z scores were additionally computed relative to the shuffle distribution.

Significant clustering was defined as a mean NN distance significantly smaller than that expected under label permutation, indicating that whisker-responsive cells were spatially closer to one another than predicted by chance given the overall cellular layout. Results were evaluated across multiple values of k ($k = 1–5$) to assess robustness across spatial scales (Supplementary Fig. 15j). When pooling data across mice, the observed mean nearest-neighbor distance for each value of k was normalized to the mean of its corresponding shuffled-label distribution within each mouse. Values below 1 therefore indicate that whisker-responsive cells were spatially closer to one another than expected under random label assignment (Supplementary Fig. 15k).

Statistics and reproducibility. No statistical method was used to predetermine sample size. Sample sizes were based on previous in vivo calcium imaging studies and are reported in the figure legends and Supplementary Data 1. Unless otherwise stated, mice were considered biological subjects and FOVs were treated as statistical units where indicated. In the Environment 2 open-field experiment, 12 FOV datasets were obtained from 10 mice because two mice underwent a second whisker-trimming experiment in newly selected FOVs after whisker regrowth. These repeated experiments are identified in the relevant figure legends and Source Data. Data were excluded only according to the predefined criteria described in the relevant Methods sections. These criteria included failure to meet predefined cell-identification criteria, missing or non-finite measurements, and failure to obtain valid matched measurements in both sessions for paired analyses. No additional data were excluded based on the statistical results.

The experiments were not randomized because animals underwent predefined experimental session sequences. The investigators were not blinded to experimental conditions during data collection or outcome assessment. However, all imaging and behavioral data were processed using the same predefined automated analysis pipelines and cell-classification criteria across experimental conditions, minimizing subjective intervention during data analysis.

Data processing and statistical analyses were performed using MATLAB R2022a, Python 3.12, and GraphPad Prism 9. Figures were generated using MATLAB, Python, and GraphPad Prism 9 and assembled in Adobe Illustrator 2024. The numerical data underlying the box plots, bar plots, scatter plots, and associated statistical analyses are provided in the Source Data files.

Reporting summary

Further information on research design is available in the Nature Portfolio Reporting Summary linked to this article.

Data availability

Example processed calcium imaging and behavioral data supporting this study have been deposited in Zenodo at https://doi.org/10.5281/zenodo.21716960. Owing to the substantial size of the raw calcium imaging and behavioral video files, the complete raw dataset has not been deposited in a public repository. Access to these data could be requested from the corresponding author. Source data underlying all statistical plots are provided with this paper. Source data are provided with this paper.

Code availability

The custom analysis code used in this study is publicly available on GitHub at https://github.com/Bluemooncell/Analysis-on-MEC-neural-Activity. The exact version of the code used to generate the results reported in this study has been archived together with the supporting processed data in Zenodo at https://doi.org/10.5281/zenodo.21716960.

References

1. Terry, A. V., Jr. Spatial navigational (water maze) tasks. In *Methods of Behavior Analysis in* Neuroscience (ed. Buccafusco, J. J.) (CRC Press, 2009).
2. Rossier, J., Haeberli, C. & Schenk, F. Auditory cues support place navigation in rats when associated with a visual cue. *Behavioural Brain Res.* **117**, 209–214 (2000).
3. Watanabe, S. & Yoshida, M. Auditory cued spatial learning in mice. *Physiol. Behav.* **92**, 906–910 (2007).
4. Bao, X. et al. Grid-like Neural Representations Support Olfactory Navigation of a Two-Dimensional Odor Space. *Neuron* **102**, 1066–1075.e1065 (2019).
5. Gener, T., Perez-Mendez, L. & Sanchez-Vives, M. V. Tactile modulation of hippocampal place fields. *Hippocampus* **23**, 1453–1462 (2013).
6. Mittelstaedt, M. L. & Mittelstaedt, H. Homing by Path Integration in a Mammal. *Naturwissenschaften* **67**, 566–567 (1980).
7. McNaughton, B. L. et al. Deciphering the hippocampal polyglot: The hippocampus as a path integration system. *J. Exp. Biol.* **199**, 173–185 (1996).
8. Touretzky, D. S. & Redish, A. D. Theory of rodent navigation based on interacting representations of space. *Hippocampus* **6**, 247–270 (1996).
9. Seelig, J. D. & Jayaraman, V. Neural dynamics for landmark orientation and angular path integration. *Nature* **521**, 186–191 (2015).
10. Perez-Escobar, J. A., Kornienko, O., Latuske, P., Kohler, L. & Allen, K. Visual landmarks sharpen grid cell metric and confer context specificity to neurons of the medial entorhinal cortex. *eLife* **5**, e16937 (2016).
11. Hardcastle, K., Ganguli, S. & Giocomo, L. M. Environmental Boundaries as an Error Correction Mechanism for Grid Cells. *Neuron* **86**, 827–839 (2015).
12. McNaughton, B. L., Battaglia, F. P., Jensen, O., Moser, E. I. & Moser, M. B. Path integration and the neural basis of the 'cognitive map'. *Nat. Rev. Neurosci.* **7**, 663–678 (2006).
13. Hafting, T., Fyhn, M., Molden, S., Moser, M. B. & Moser, E. I. Microstructure of a spatial map in the entorhinal cortex. *Nature* **436**, 801–806 (2005).
14. Sargolini, F. et al. Conjunctive representation of position, direction, and velocity in entorhinal cortex. *Science* **312**, 758–762 (2006).
15. Savelli, F., Yoganarasimha, D. & Knierim, J. J. Influence of boundary removal on the spatial representations of the medial entorhinal cortex. *Hippocampus* **18**, 1270–1282 (2008).
16. Solstad, T., Boccara, C. N., Kropff, E., Moser, M. B. & Moser, E. I. Representation of Geometric Borders in the Entorhinal Cortex. *Science* **322**, 1865–1868 (2008).
17. Diehl, G. W., Hon, O. J., Leutgeb, S. & Leutgeb, J. K. Grid and Nongrid Cells in Medial Entorhinal Cortex Represent Spatial Location and Environmental Features with Complementary Coding Schemes. *Neuron* **94**, 83–92 (2017).
18. Kropff, E., Carmichael, J. E., Moser, M. B. & Moser, E. I. Speed cells in the medial entorhinal cortex. *Nature* **523**, 419–424 (2015).
19. Hinman, J. R., Brandon, M. P., Climer, J. R., Chapman, G. W. & Hasselmo, M. E. Multiple Running Speed Signals in Medial Entorhinal Cortex. *Neuron* **91**, 666–679 (2016).
20. Munn, R. G. K., Mallory, C. S., Hardcastle, K., Chetkovich, D. M. & Giocomo, L. M. Entorhinal velocity signals reflect environmental geometry. *Nat. Neurosci.* **23**, 239–251 (2020).
21. Chen, G., Manson, D., Cacucci, F. & Wills, T. J. Absence of Visual Input Results in the Disruption of Grid Cell Firing in the Mouse. *Curr. Biol.: CB* **26**, 2335–2342 (2016).
22. Taube, J. S., Muller, R. U. & Ranck, J. B. Jr Head-direction cells recorded from the postsubiculum in freely moving rats. II. Effects of environmental manipulations. *J. Neurosci.* **10**, 436–447 (1990).
23. Zugaro, M. B., Arleo, A., Berthoz, A. & Wiener, S. I. Rapid spatial reorientation and head direction cells. *J. Neurosci.* **23**, 3478–3482 (2003).
24. Dannenberg, H., Lazaro, H., Nambiar, P., Hoyland, A. & Hasselmo, M. E. Effects of visual inputs on neural dynamics for coding of location and running speed in medial entorhinal cortex. *eLife* **9**, e62500 (2020).
25. Adibi, M. Whisker-Mediated Touch System in Rodents: From Neuron to Behavior. *Front Syst. Neurosci.* **13**, 40 (2019).
26. Vincent, S. B. *The Functions of the Vibrissae in the Behavior of the White Rat*. Vol. 1 (University of Chicago, 1912).
27. Pereira, A. et al. Processing of tactile information by the hippocampus. *Proc. Natl. Acad. Sci. USA* **104**, 18286–18291 (2007).
28. Knutsen, P. M., Pietr, M. & Ahissar, E. Haptic object localization in the vibrissal system: behavior and performance. *J. Neurosci.* **26**, 8451–8464 (2006).
29. Hutson, K. A. & Masterton, R. B. The sensory contribution of a single vibrissa's cortical barrel. *J. Neurophysiol.* **56**, 1196–1223 (1986).
30. Jenkinson, E. W. & Glickstein, M. Whiskers, barrels, and cortical efferent pathways in gap crossing by rats. *J. Neurophysiol.* **84**, 1781–1789 (2000).
31. Prigg, T., Goldreich, D., Carvell, G. E. & Simons, D. J. Texture discrimination and unit recordings in the rat whisker/barrel system. *Physiol. Behav.* **77**, 671–675 (2002).
32. Von Heimendahl, M., Itskov, P. M., Arabzadeh, E. & Diamond, M. E. Neuronal activity in rat barrel cortex underlying texture discrimination. *PLoS Biol.* **5**, 2696–2708 (2007).
33. Chapin, J. K. & Lin, C. S. Mapping the Body Representation in the Si Cortex of Anesthetized and Awake Rats. *J. Comp. Neurol.* **229**, 199–213 (1984).

34. Haidarliu, S., Kleinfeld, D. & Ahissar, E. Mediation of muscular control of rhinarial motility in rats by the nasal cartilaginous skeleton. *Anat. Rec. (Hoboken)* **296**, 1821–1832 (2013).
35. Zong, W. J. et al. Miniature two-photon microscopy for enlarged field-of-view, multi-plane and long-term brain imaging. *Nat. Methods* **18**, 46–49 (2021).
36. Asumbisa, K., Peyrache, A. & Trenholm, S. Flexible cue anchoring strategies enable stable head direction coding in both sighted and blind animals. *Nat. Commun.* **13**, 5483 (2022).
37. Asumbisa, K., Peyrache, A. & Trenholm, S. Stereo olfaction underlies stable coding of head direction in blind mice. *Nat. Commun.* **16**, 3545 (2025).
38. Bassett, J. P. & Taube, J. S. Neural correlates for angular head velocity in the rat dorsal tegmental nucleus. *J. Neurosci.* **21**, 5740–5751 (2001).
39. Graham, J. A. et al. Angular Head Velocity Cells within Brainstem Nuclei Projecting to the Head Direction Circuit. *J. Neurosci.* **43**, 8403–8424 (2023).
40. Fuhs, M. C. & Touretzky, D. S. A spin glass model of path integration in rat medial entorhinal cortex. *J. Neurosci.* **26**, 4266–4276 (2006).
41. Obenhaus, H. A. et al. Functional network topography of the medial entorhinal cortex. *Proc. Natl. Acad. Sci. USA* **119**, e2121655119 (2022).
42. Wallach, A., Bagdasarian, K. & Ahissar, E. On-going computation of whisking phase by mechanoreceptors. *Nat. Neurosci.* **19**, 487–493 (2016).
43. Moser, M. B., Rowland, D. C. & Moser, E. I. Place cells, grid cells, and memory. *Cold Spring Harb. Perspect. Biol.* **7**, a021808 (2015).
44. Taube, J. S., Muller, R. U. & Ranck, J. B. Jr Head-direction cells recorded from the postsubiculum in freely moving rats. I. Description and quantitative analysis. *J. Neurosci.* **10**, 420–435 (1990).
45. Stackman, R. W. & Taube, J. S. Firing properties of head direction cells in the rat anterior thalamic nucleus: dependence on vestibular input. *J. Neurosci.* **17**, 4349–4358 (1997).
46. Stackman, R. W., Clark, A. S. & Taube, J. S. Hippocampal spatial representations require vestibular input. *Hippocampus* **12**, 291–303 (2002).
47. Olsen, G. M., Ohara, S., Iijima, T. & Witter, M. P. Parahippocampal and retrosplenial connections of rat posterior parietal cortex. *Hippocampus* **27**, 335–358 (2017).
48. Shao, Q. et al. A non-canonical visual cortical-entorhinal pathway contributes to spatial navigation. *Nat. Commun.* **15**, 4122 (2024).
49. Ajabi, Z., Keinath, A. T., Wei, X. X. & Brandon, M. P. Population dynamics of head-direction neurons during drift and reorientation. *Nature* **615**, 892–899 (2023).
50. Sit, K. K. & Goard, M. J. Coregistration of heading to visual cues in retrosplenial cortex. *Nat. Commun.* **14**, 1992 (2023).
51. Mizumori, S. J. Y. & Williams, J. D. Directionally Selective Mnemonic Properties of Neurons in the Lateral Dorsal Nucleus of the Thalamus of Rats. *J. Neurosci.* **13**, 4015–4028 (1993).
52. Zhang, K. Representation of spatial orientation by the intrinsic dynamics of the head-direction cell ensemble: A theory. *J. Neurosci.* **16**, 2112–2126 (1996).
53. Towal, R. B. & Hartmann, M. J. Right-left asymmetries in the whisking behavior of rats anticipate head movements. *J. Neurosci.* **26**, 8838–8846 (2006).
54. Meyer, A. F., O'Keefe, J. & Poort, J. Two Distinct Types of Eye-Head Coupling in Freely Moving Mice. *Curr. Biol.* **30**, 2116–2130 (2020).
55. Michaiel, A. M., Abe, E. T. & Niell, C. M. Dynamics of gaze control during prey capture in freely moving mice. *eLife* **9**, e57458 (2020).
56. Mallory, C. S. et al. Mouse entorhinal cortex encodes a diverse repertoire of self-motion signals. *Nat. Commun.* **12**, 671 (2021).
57. Spalla, D., Treves, A. & Boccara, C. N. Angular and linear speed cells in the parahippocampal circuits. *Nat. Commun.* **13**, 1907 (2022).
58. Aronov, D. & Tank, D. W. Engagement of Neural Circuits Underlying 2D Spatial Navigation in a Rodent Virtual Reality System. *Neuron* **84**, 442–456 (2014).
59. Handler, A. & Ginty, D. D. The mechanosensory neurons of touch and their mechanisms of activation. *Nat. Rev. Neurosci.* **22**, 521–537 (2021).
60. Brandon, M. P. et al. Reduction of Theta Rhythm Dissociates Grid Cell Spatial Periodicity from Directional Tuning. *Science* **332**, 595–599 (2011).
61. Winter, S. S., Mehlman, M. L., Clark, B. J. & Taube, J. S. Passive Transport Disrupts Grid Signals in the Parahippocampal Cortex. *Curr. Biol.* **25**, 2493–2502 (2015).
62. Welker, W. I. Analysis of sniffing of the albino rat. *Behaviour* **22**, 223–244 (1964).
63. Crochet, S. & Petersen, C. C. H. Correlating whisker behavior with membrane potential in barrel cortex of awake mice. *Nat. Neurosci.* **9**, 608–610 (2006).
64. Krupa, D. J., Matell, M. S., Brisben, A. J., Oliveira, L. M. & Nicolelis, M. A. Behavioral properties of the trigeminal somatosensory system in rats performing whisker-dependent tactile discriminations. *J. Neurosci.* **21**, 5752–5763 (2001).
65. Le Merre, P. et al. Reward-Based Learning Drives Rapid Sensory Signals in Medial Prefrontal Cortex and Dorsal Hippocampus Necessary for Goal-Directed Behavior. *Neuron* **97**, 83–91.e5 (2018).
66. Gonzalez-Perez, O., López-Virgen, V. & Ibarra-Castaneda, N. Permanent Whisker Removal Reduces the Density of c-Fos+ Cells and the Expression of Calbindin Protein, Disrupts Hippocampal Neurogenesis and Affects Spatial-Memory-Related Tasks. *Front Cell Neurosci.* **12**, 132 (2018).
67. Burwell, R. D. & Amaral, D. G. Cortical afferents of the perirhinal, postrhinal, and entorhinal cortices of the rat. *J. Comp. Neurol.* **398**, 179–205 (1998).
68. Burwell, R. D. & Amaral, D. G. Perirhinal and postrhinal cortices of the rat: Interconnectivity and connections with the entorhinal cortex. *J. Comp. Neurol.* **391**, 293–321 (1998).
69. Agster, K. L. & Burwell, R. D. Hippocampal and subicular efferents and afferents of the perirhinal, postrhinal, and entorhinal cortices of the rat. *Behavioural Brain Res.* **254**, 50–64 (2013).
70. Diamond, M. E., von Heimendahl, M., Knutsen, P. M., Kleinfeld, D. & Ahissar, E. Where" and "what" in the whisker sensorimotor system. *Nat. Rev. Neurosci.* **9**, 601–612 (2008).
71. Kitanishi, T. & Matsuo, N. Organization of the Claustrum-to-Entorhinal Cortical Connection in Mice. *J. Neurosci.* **37**, 269–280 (2017).
72. Low, R. J., Gu, Y. & Tank, D. W. Cellular resolution optical access to brain regions in fissures: imaging medial prefrontal cortex and grid cells in entorhinal cortex. *Proc. Natl. Acad. Sci. USA* **111**, 18739–18744 (2014).
73. Mathis, A. et al. DeepLabCut: markerless pose estimation of user-defined body parts with deep learning. *Nat. Neurosci.* **21**, 1281–1289 (2018).
74. Nath, T. et al. Using DeepLabCut for 3D markerless pose estimation across species and behaviors. *Nat. Protoc.* **14**, 2152–2176 (2019).
75. Insafutdinov, E., Pishchulin, L., Andres, B., Andriluka, M. & Schiele, B. in *Computer Vision–ECCV 2016: 14th European Conference, Amsterdam, The Netherlands*, 2016, *Proceedings, Part VI 14*. 34–50 (Springer).
76. Lever, C., Burton, S., Jeewajee, A., O'Keefe, J. & Burgess, N. Boundary Vector Cells in the Subiculum of the Hippocampal Formation. *J. Neurosci.* **29**, 9771–9777 (2009).
77. Hartley, T., Lever, C., Burgess, N. & O'Keefe, J. Space in the brain: how the hippocampal formation supports spatial cognition. *Philos. T R. Soc. B* **369**, 20120510 (2014).
78. Zhang, S. J. Optogenetic dissection of entorhinal-hippocampal functional connectivity. *Science* **340**, 273–273 (2013).

79. Pachitariu, M. et al. Suite2p: beyond 10,000 neurons with standard two-photon microscopy. *bioRxiv* 061507 (2016).
80. Chen, T. W. et al. Ultrasensitive fluorescent proteins for imaging neuronal activity. *Nature* **499**, 295–300 (2013).
81. Zong, W. J. et al. Large-scale two-photon calcium imaging in freely moving mice. *Cell* **185**, 1240–1256 (2022).
82. Friedrich, J. & Paninski, L. Fast Active Set Methods for Online Spike Inference from Calcium Imaging. *Adv. Neural. Inf. Process Syst.* **29** (2016).
83. Pnevmatikakis, E. A. et al. Simultaneous Denoising, Deconvolution, and Demixing of Calcium Imaging Data. *Neuron* **89**, 285–299 (2016).
84. Skaggs, W., Mcnaughton, B. & Gothard, K. An information-theoretic approach to deciphering the hippocampal code. *Adv. Neural. Inf. Process. Syst.* **5** (1992).
85. Fitzgibbon, A., Pilu, M. & Fisher, R. B. Direct least square fitting of ellipses. *IEEE Trans. Pattern Anal. Mach. Intell.* **21**, 476–480 (1999).
86. Zhang, K., Ginzburg, I., McNaughton, B. L. & Sejnowski, T. J. Interpreting neuronal population activity by reconstruction: unified framework with application to hippocampal place cells. *J. Neurophysiol.* **79**, 1017–1044 (1998).
87. Pettit, N. L., Yuan, X. C. & Harvey, C. D. Hippocampal place codes are gated by behavioral engagement. *Nat. Neurosci.* **25**, 561–566 (2022).
88. Fisher, R. A. The use of multiple measurements in taxonomic problems. *Ann. Eugen.* **7**, 179–188 (1936).
89. Syeda, A. et al. Facemap: a framework for modeling neural activity based on orofacial tracking. *Nat. Neurosci.* **27**, 187–195 (2024).

Acknowledgements

We are grateful to the National Center for Protein Sciences at Peking University in Beijing, China, for their support with imaging and histology. We thank Emilio Kropff, Xiang Zhang and Meng Zhong for their invaluable guidance on experiment techniques and data processing during the early stages of this project.

Author contributions

J.T. and C.M. designed research, J.T, N.H. and Y.H. collected the data, J.T., S.W., Y.Z., X.Z., Y.L. and Z.W. performed the surgeries, J.T. analyzed the data. Y.Z. set up the hardware for the whisker-related experiments. S.Y. developed the LDA-related algorithm. C.M. supervised the project, J.T. and C.M. wrote the paper with input from all authors.

Funding

This research was funded by the Science Fund for Distinguished Young Scholars of Beijing (JQ23023; C.M.), the Qidong-SLS Innovation Fund (2023002029 and 2020001540; C.M.), the Space Brain Project of Lingang Laboratory (Grant No. LG-TKN-202204-01; C.M.), the Chinese Government Foreign Expert Project for Emilio Kropff (G2022101003L; C.M.), and the PICT-2019-2596 grant from the Argentine Ministry of Science (E.K.).

Competing interests

The authors declare no competing interests.

Additional information

Supplementary information The online version contains supplementary material available at https://doi.org/10.1038/s41467-026-78000-2.

Correspondence and requests for materials should be addressed to Chenglin Miao.

Peer review information *Nature Communications* thanks Sami El-Boustani and the other anonymous reviewer(s) for their contribution to the peer review of this work. A peer review file is available.

Reprints and permissions information is available at http://www.nature.com/reprints

Publisher's note Springer Nature remains neutral with regard to jurisdictional claims in published maps and institutional affiliations.

Open Access This article is licensed under a Creative Commons Attribution-NonCommercial-NoDerivatives 4.0 International License, which permits any non-commercial use, sharing, distribution and reproduction in any medium or format, as long as you give appropriate credit to the original author(s) and the source, provide a link to the Creative Commons licence, and indicate if you modified the licensed material. You do not have permission under this licence to share adapted material derived from this article or parts of it. The images or other third party material in this article are included in the article's Creative Commons licence, unless indicated otherwise in a credit line to the material. If material is not included in the article's Creative Commons licence and your intended use is not permitted by statutory regulation or exceeds the permitted use, you will need to obtain permission directly from the copyright holder. To view a copy of this licence, visit http://creativecommons.org/licenses/by-nc-nd/4.0/.

© The Author(s) 2026

This Article in Press is shared early to give you faster access to new research. It is citable and carries a permanent DOI. The final edited version will replace it automatically.